Abteilung Quanteninformationsverarbeitung der Universität Ulm

The Rotational Doppler Effect and the Rotational Frequency Shift



Dissertation zur Erlangung des Doktorgrades Dr. rer. nat.
der Fakultät für Naturwissenschaften der Universität Ulm
vorgelegt von

Marcin Michalski aus Sosnowiec

2004

Amtierender Dekan:	Prof. Dr. R. J. Behm
1. Gutachter:	Prof. Dr. W. Hüttner
2. Gutachter:	Prof. Dr. W. Schleich
3. Gutachter:	Prof. dr hab. I. Białynicki-Birula

Tag der mündlichen Prüfung: 25.6.2004

Contents

1 Introduction **5**

2 Classical Rotational Doppler Effect (RDE) **7**
2.1 Transformation of the electromagnetic wave 7
2.2 RDE in the literature 9
2.3 Observation of the classical RDE 9

3 Quantum systems in the rotating frame **14**
3.1 Rotational Frequency Shift (RFS) - Basic considerations 14
3.2 Two-level atom in the rotating frame 16
3.3 Three-level atom in the rotating frame 17
3.3.1 Traditional view - Dynamic Stark Effect 18
3.3.2 Rotating frame approach 19
3.4 Theory of the intermediate RFS in a molecular system 21

4 Experimental **25**
4.1 Laser spectroscopic means 25
4.2 Fast rotation RFS in atomic lithium 25
4.2.1 Apparatus 25
4.2.2 Results 28
4.3 Intermediate RFS in H_2CS molecules 30
4.3.1 Some properties of thioformaldehyde 30
4.3.2 Apparatus 32
4.3.3 Results 34

5 Relation of the RFS to some other effects **38**
5.1 Berry Phase 38
5.1.1 Quadrupole nuclear resonance with a rotating sample - strong field RFS 40
5.2 The dressed state approach 42
5.3 Rotation as a fictitious magnetic field 43
5.4 Sagnac Effect 43

Summary **45**

Zusamenfassung **46**

A Experimental details **47**
A.1 Evaluation of the effect-modulation signals 47
A.2 Production of circularly polarized light 48
A.3 Production of the rotating electric field 49

Chapter 1

Introduction

The translative Doppler effect [1] is a well known phenomenon. Much less and not *explicitly* known for a long time was the rotational Doppler effect [3, 4]. From a descriptive point of view the rotational Doppler effect (RDE) arises, similarly to the translative one, from the transformation between different frames. There are, however, some differences:

- at least one frame is non-inertial, which leads to dynamical effects,
- the rotational Doppler effect takes place only for waves (or fields) possessing angular momentum, i. e. vector or tensor waves. No effect takes place for waves showing rotational symmetry around the propagation direction, for example planar longitudinal sound waves,
- the rotational Doppler effect is proportional solely to the transformation parameter, the rotational frequency, as long as dynamical effects can be neglected. This differs from the translative Doppler effect, where the frequency shift is also proportional to the frequency of the wave itself.

The rotational frequency shift (RFS) has recently been discovered by I. Białynicki-Birula and Z. Białynicka-Birula [2]. It takes place when a quantum system is put in a rotating environment, say field. As the hamiltonian of such a system is time dependent, it is impossible to define stationary energy levels. But there exists the frame co-rotating with the field, where the field is constant. It is convenient to consider the system in this rotating frame where the time-independent Schrödinger equation can be solved. There are two parameters important for the RFS, namely the rotational frequency and the coupling strength between the external field and the quantum system. Depending on the quantitative relation between the coupling energy, $\langle\Psi|\,\mu\,|\Psi\rangle$, and the driving angular energy $\hbar\Omega$, one can mark out three cases:

- the *fast rotation* case where $\langle\Psi|\,\mu\,|\Psi\rangle \ll \hbar\Omega$,

- the *strong field* case when $\langle\Psi|\,\mu\,|\Psi\rangle \gg \hbar\Omega$, and
- the most interesting *intermediate* case, where both parameters are comparable in magnitude.

The arrangement of this dissertation is as following: In chapter 2 the rotational Doppler effect of the electromagnetic wave is considered, theoretically and experimentally. Chapter 3 describes the Schrödinger equation in the rotating frame. The theoretical approach in chapters 2 and 3 is simple and straight-forward. I decided to treat the transformation of the electromagnetic wave, the driving field leading to the rotational frequency shift, classically and separated from the quantum system acted on by the field. A more elegant quantum mechanical treatment of the RFS is provided in [2]. Chapter 4 describes the main part of this work, the high resolution laser experiments demonstrating the existence of RFS in atomic and molecular physics. There are some phenomena described in the literature which can be re-interpreted in terms of a RFS, such as quadrupole nuclear resonance in a rotating sample, the Sagnac effect or the fictitious magnetic field. These will be discussed in chapter 5.

Chapter 2

Classical Rotational Doppler Effect (RDE)

2.1 Transformation of the electromagnetic wave

We consider an electromagnetic wave propagating along the z-direction in the frame O:

$$E_x = E_0 \sin(kz - \omega t), \tag{2.1}$$

$$E_y = \pm E_0 \cos(kz - \omega t), \tag{2.2}$$

where $\pm$ is for left- or right-handed circular polarization. Let the frame O' rotate relative to O with frequency Ω, see fig. 2.1. In a classical, non-relativistic transformation, coordinates in the frame O' are

$$x' = x\cos\Omega t - y\cos\Phi\sin\Omega t + z\sin\Phi\sin\Omega t, \tag{2.3}$$

$$y' = x\sin\Omega t + y\cos\Phi\cos\Omega t - z\sin\Phi\cos\Omega t, \tag{2.4}$$

$$z' = y\sin\Phi + z\cos\Phi, \tag{2.5}$$

where Φ is the angle between z (wave propagation direction) and z' (axis of rotation) in the yz plane. What is the frequency ω' in the frame O'? Restricting the consideration to the rotation axis we have

$$E'_x = E_x\cos\Omega t - E_y\cos\Phi\sin\Omega t + E_z\sin\Phi\sin\Omega t, \tag{2.6}$$

$$E'_y = E_x\sin\Omega t + E_y\cos\Phi\cos\Omega t - E_z\sin\Phi\cos\Omega t, \tag{2.7}$$

$$E'_z = E_y\sin\Phi + E_z\cos\Phi, \tag{2.8}$$

or using eqs. 2.1 and 2.2

$$E'_x = \frac{1}{2}E_0\sin(kz - \omega t + \Omega t)(1 \mp \cos\Phi) +$$

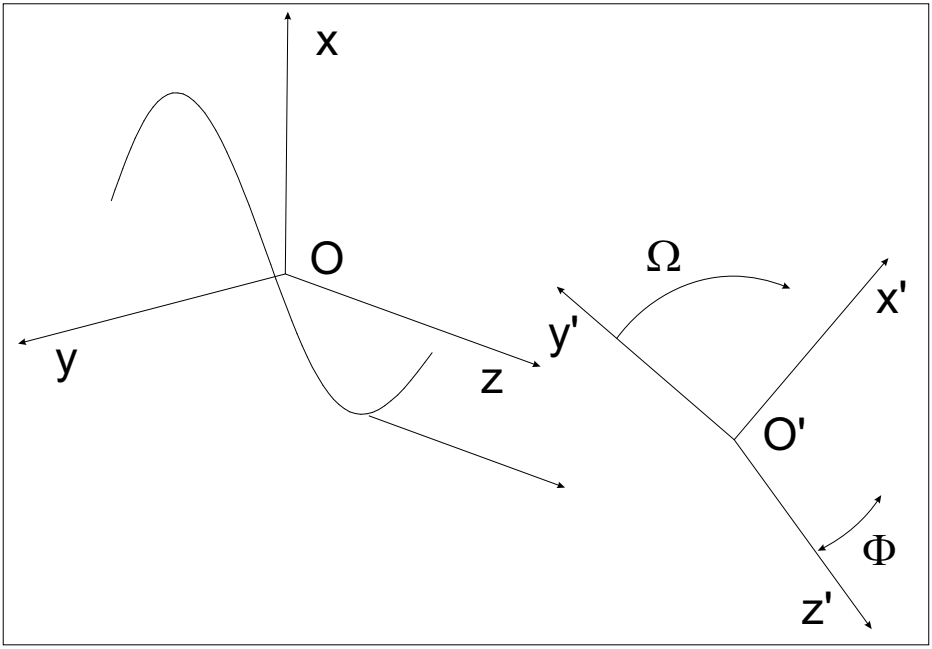

Figure 2.1: Frames O and O'. The frame origins are shifted against each other in order to avoid confusion.

$$\frac{1}{2}E_0 \sin(kz - \omega t - \Omega t)(1 \pm \cos\Phi), \tag{2.9}$$

$$E'_y = \frac{1}{2}E_0 \cos(kz - \omega t - \Omega t)(1 \pm \cos\Phi) -$$

$$\frac{1}{2}E_0 \cos(kz - \omega t + \Omega t)(1 \mp \cos\Phi). \tag{2.10}$$

As a special case, we choose the rotation axis parallel to the propagation direction ($\Phi = 0$):

$$E'_x = E_0 \sin\left(kz - (\omega \pm \Omega)t\right) \tag{2.11}$$

$$E'_y = E_0 \cos\left(kz - (\omega \pm \Omega)t\right) \tag{2.12}$$

So the frequency ω' in the frame O' :

$$\omega' = \omega \pm \Omega \tag{2.13}$$

is shifted, depending on the polarization direction. The frequency of a linearly polarized wave would be split, because it consists of two coherent circular polarized waves with opposite sign, and the frequency of each of these components is

shifted in the other direction. Another special case occurs when the field oscillates along the rotation axis, like the magnetic field in the experiment described in [28]. Here no frequency change is observed as considered in more detail in sec. 5.1.1 below.

2.2 RDE in the literature

There are recent experiments showing the existence of the classical (kinetic) rotational Doppler effect (RDE), for example in [3, 4]. In these experiments the light beam was guided through rotating elements which affected the angular momentum, the photon spin in the case of circular polarization as well as the orbital angular momentum [5]. The RDE is also of importance in the radio communication with spacecrafts. This was realized first in the early interplanetary missions PIONEER 10/11 [6, 7] many years after theirs launches [7]. The present author contributed to the recent discussion about the anomalous acceleration of these spacecrafts [8]. The rotational Doppler effect also shows up in the high precision satellite navigation system GPS as the so-called *phase wrap-up* [9].

2.3 Observation of the classical RDE

The present author has previously demonstrated the classical RDE in his M. Sc. thesis using electromagnetic circuit equipment [26]. The results are briefly shown here.

In this experiment a low-frequency electromagnetic field is emitted by the source at rest while the detector is rotating. The main element of the experimental setup (fig. 2.2) is an electric motor (from an old commercial kitchen vacuum cleaner). The coils of the motor are fixed. They produce time varying magnetic fields. The detector, a coil, is fastened to the rotor which provides the frequency of the rotating frame. The axis of the coil is perpendicular to the rotation axis. The detector signal is fed through to the amplifier by a rotatable connector. A standard stereo sound amplifier has been employed for this purpose. The amplified signal is recorded by the computer via its standard sound card (microphone input) with 8-Bit resolution and 22.05 kHz sampling rate.

The first measurement has been performed holding rotor (and detector) at rest[1]. Figure 2.3 shows the recorded signal and the associated power spectrum (square of the Fourier transform) of the signal in arbitrary units (which are, however, the same for both figures). The 50 Hz net frequency and some odd harmonics are well resolved. The origin of the higher order frequencies is not

[1] The motor is designed for a three-phase electrical power line. However, it can be used with a standard home one-phase one when a proper phase shift is provided between two of the three input connectors as shown on figure 2.2. One can adjust the power of such a motor by means of a variable condenser capacity. The torque was kept low to allow for an easy control of the rotation frequency, by friction.

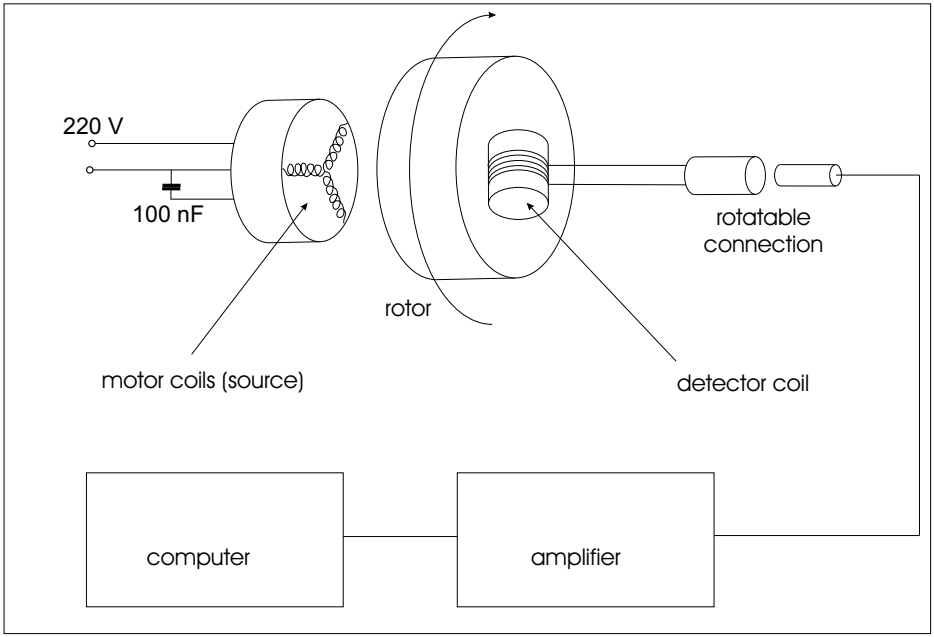

Figure 2.2: Experimental setup for demonstrating the classical Doppler effect.

clear, but they must be caused by the motor coils. The same signal is observed when the rotor is removed and the detector put just near the motor. Figures 2.4 and 2.5 show the signals and spectra when the detector was rotating with frequencies of approximately 3 and 10 Hz, respectively. The spectral lines split when the detector is rotating. It is seen that the intensities of the split lines are not equal, and that the relation between lower- and higher-frequency shifted components is different for each frequency component. This is caused by the variant polarization of the frequency components of the source field. Especially the strong asymmetry of the 50 Hz component splitting is due to the fact that the motor coils generate a field which is nearly circularly polarized. The experimental results agree with the theory described in section 2.1.

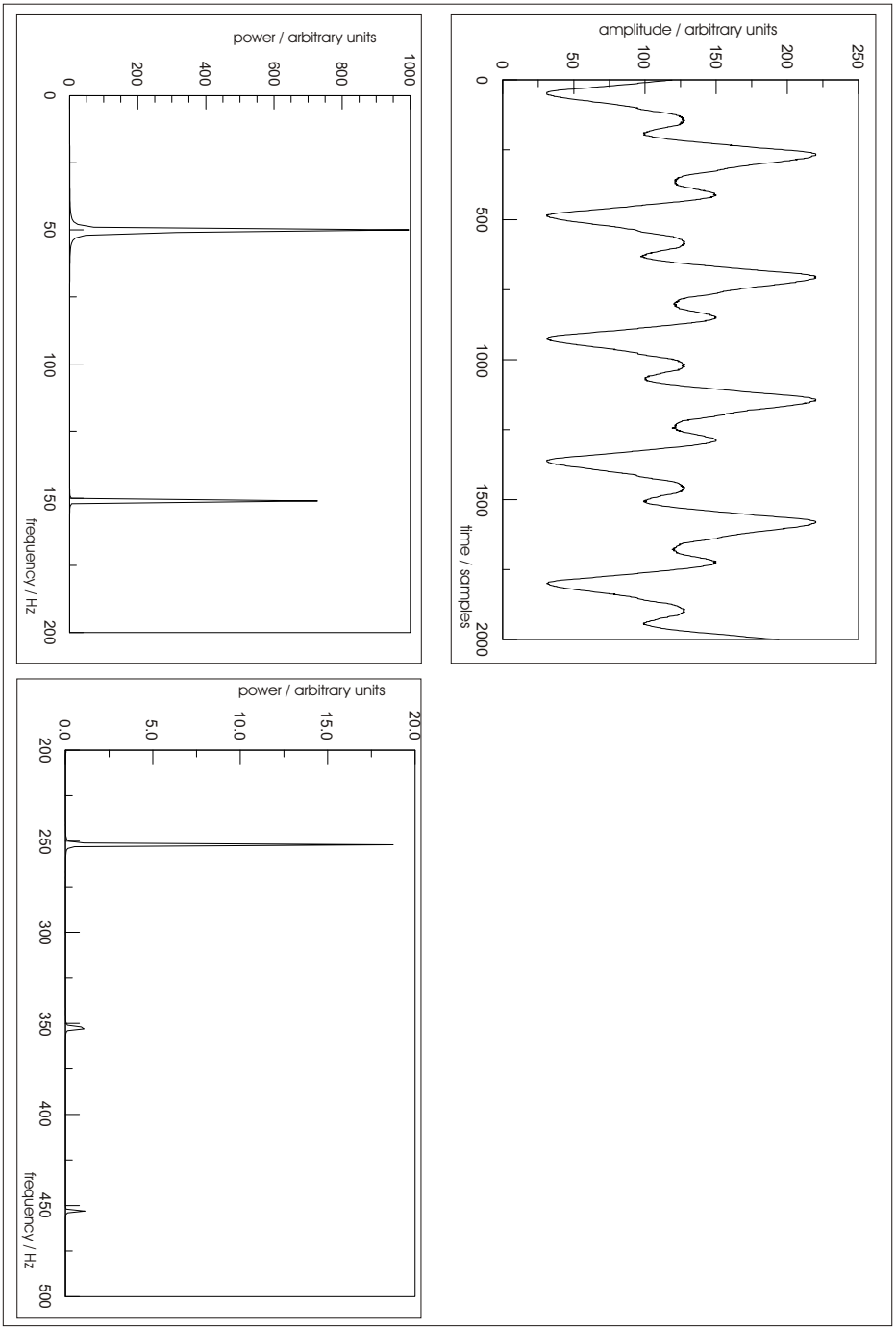

Figure 2.3: Signal and its spectrum recorded by the detector at rest.

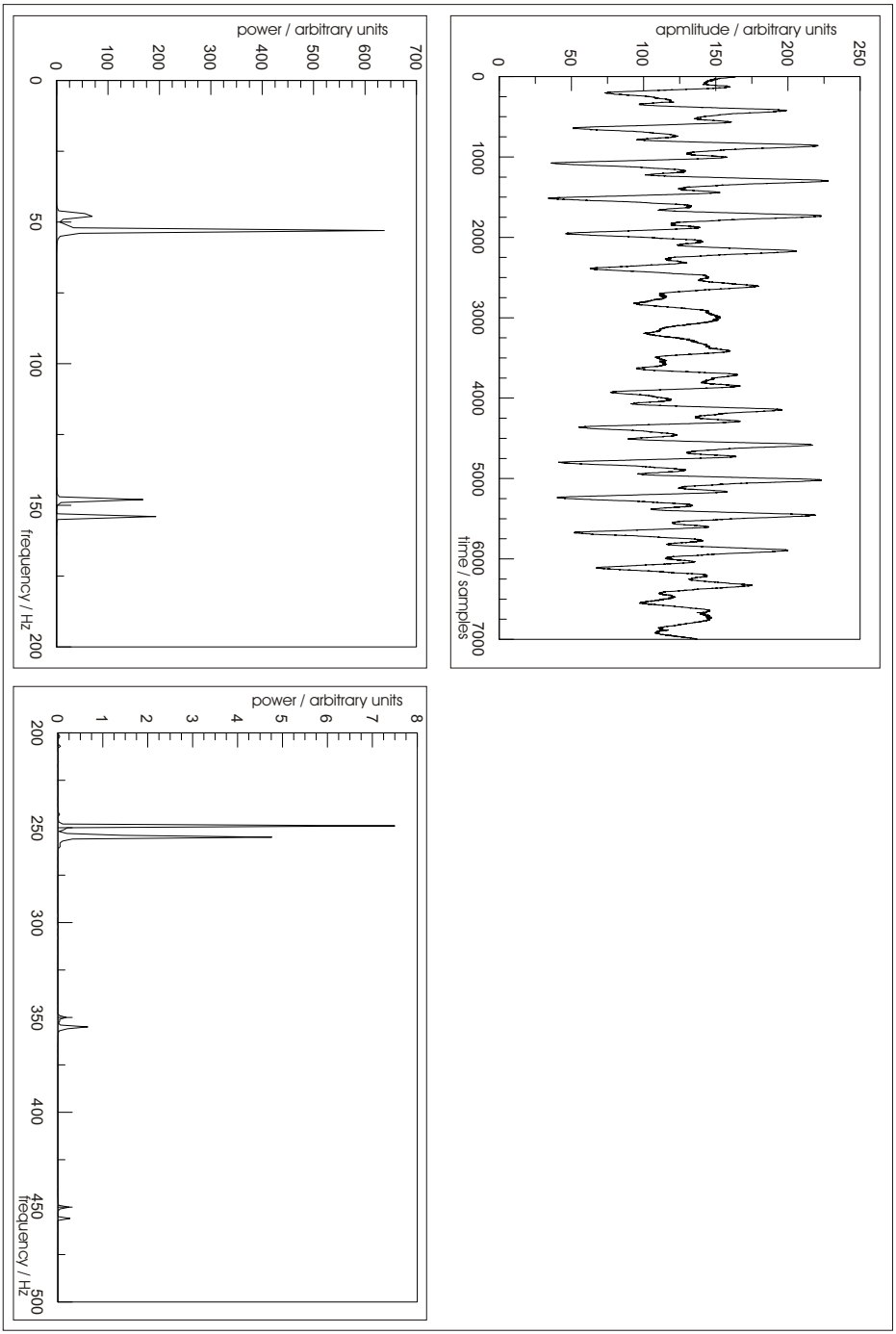

Figure 2.4: Signal and its spectrum collected with 3 Hz rotation.

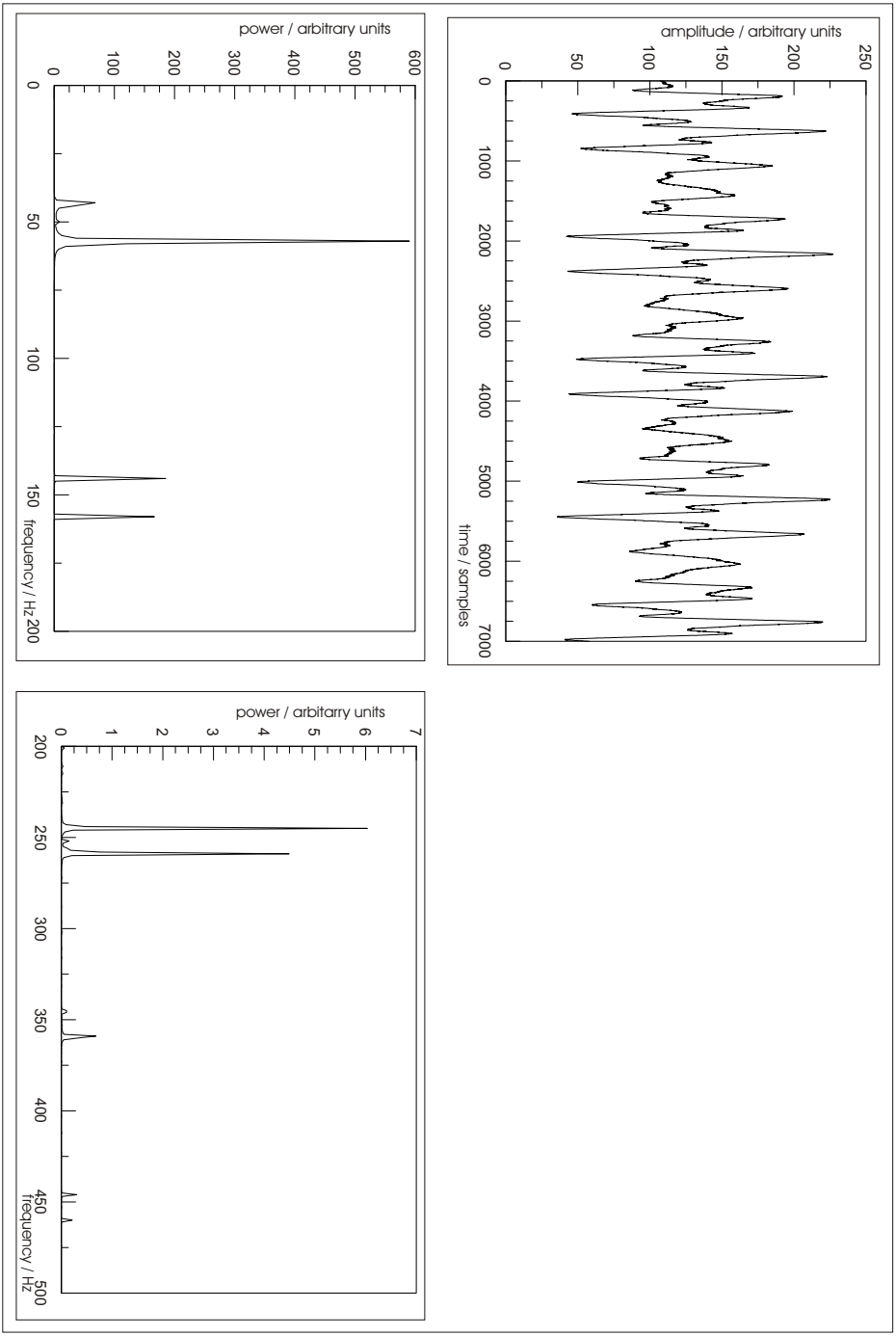

Figure 2.5: Signal and its spectrum collected with 10 Hz rotation.

Chapter 3

Quantum systems in the rotating frame

3.1 Rotational Frequency Shift (RFS) - Basic considerations

Let us consider a quantum system in the laboratory frame O. It is governed by the Schrödinger equation:

$$i\hbar\frac{\partial}{\partial t}\Psi = H\Psi, \tag{3.1}$$

where the hamiltonian, $H = H(x, y, z, t)$, is time dependent because of an interaction with a rotating external field. That means that one cannot define real energy levels [32]. But the hamiltonian is time independent in the frame O' which rotates with frequency Ω:

$$H(x', y', z', t') = H(x', y', z') = const. \tag{3.2}$$

It is, therefore, convenient to first solve the problem in the frame O'. Coordinates in the frame O' are:

$$x' = x\cos\Omega t + y\sin\Omega t, \tag{3.3}$$

$$y' = -x\sin\Omega t + y\cos\Omega t, \tag{3.4}$$

$$z' = z, \tag{3.5}$$

$$t' = t, \tag{3.6}$$

so the laplacian looks the same in frames O and O',

$$\triangle = \frac{\partial^2}{\partial x^2} + \frac{\partial^2}{\partial y^2} + \frac{\partial^2}{\partial z^2} = \frac{\partial^2}{\partial x'^2} + \frac{\partial^2}{\partial y'^2} + \frac{\partial^2}{\partial z'^2} = \triangle'. \tag{3.7}$$

But

$$\frac{\partial}{\partial t} = \frac{\partial}{\partial t'} + \Omega y' \frac{\partial}{\partial x'} - \Omega x' \frac{\partial}{\partial y'}, \tag{3.8}$$

$$i\hbar \frac{\partial}{\partial t} = i\hbar \frac{\partial}{\partial t'} + \Omega \left(x' p'_y - y' p'_x \right) = i\hbar \frac{\partial}{\partial t'} + \Omega L'_z, \tag{3.9}$$

so the Schrödinger equation in the frame O' reads

$$i\hbar \frac{\partial}{\partial t'} \Psi' = \left(H(x', y', z') - \Omega L'_z \right) \Psi' = H' \Psi', \tag{3.10}$$

where

$$H' = H(x', y', z') - \Omega L'_z. \tag{3.11}$$

Now one can solve the eigenvalue problem:

$$H' \Psi' = E' \Psi' \tag{3.12}$$

for the modified hamiltonian H'. Note that there is no implicit time dependency in equation 3.12 above.

The motivation for applying this geometric transformation into the rotating frame is similar to the one behind the dressed state or fictitious magnetic field approaches, see chapter 5. The aim is to get rid of the time-dependency of the hamiltonian.

If one considers the case of a spin-less electron, only the electronic angular momentum component, L'_z, appears in equation 3.11 for the transformed hamiltonian. In general, the term $-i\hbar(x\frac{\partial}{\partial y} - y\frac{\partial}{\partial x})$ is the z component of the *total* angular momentum operator and applies to any wave function of the rotating quantum system like of an electron or the nuclear frame of a molecule (compare sec. 5.3 and [2]).

A more elegant and general consideration can be found in [2]. The hamiltonian there

$$H(t) = \frac{1}{2}\mathbf{p}^2 + V(t) + H_F + H_I, \tag{3.13}$$

contains the electromagnetic field operator

$$H_F = \frac{1}{2} \int d^3x (\mathbf{D}^2/\epsilon_0 + \mathbf{B}^2/\mu_0), \tag{3.14}$$

and the interaction hamiltonian

$$H_I = \mathbf{p} \cdot \mathbf{A}(\mathbf{r}) + \frac{1}{2}\mathbf{A}^2(\mathbf{r}), \tag{3.15}$$

where $\mathbf{A}$ is the vector potential, $\mathbf{D}/\epsilon_0$ and $\mathbf{B}$ are the electric and magnetic field components, respectively, and $\mathbf{p}$ is the linear electronic momentum.

This incorporates the transformation of the electromagnetic field (rotational Doppler effect) into a quantum point of view. In the present work, however, the electromagnetic field transformation is considered classically, see sec. 2.1.

3.2 Two-level atom in the rotating frame

Consider the ground state $\Psi_S = |S\rangle$ and excited state $\Psi_P = |P\rangle$ of an alkali atom, disregarding electronic and nuclear spins. As the Ψ_P state possesses angular momentum, there are energetically degenerated substates with different m_L quantum numbers (angular momentum projection on the quantization axis z). A resonant electromagnetic field is applied, which causes transitions between the

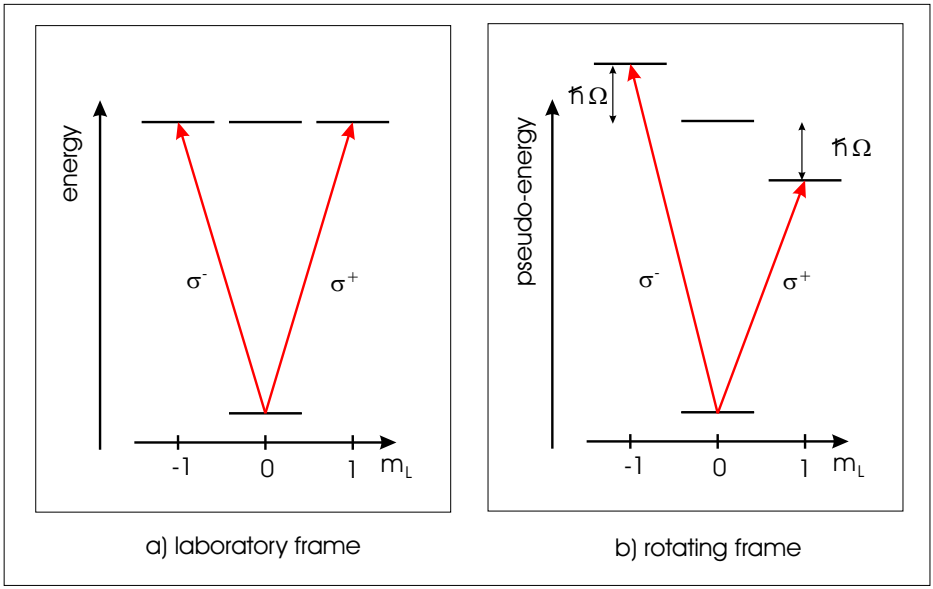

Figure 3.1: Two-level atom considered in the laboratory and rotating frames.

Ψ_S and Ψ_P levels. The Ψ_P substates involved depend on the polarization of the irradiated light, as shown on figure 3.1a. We assume the electromagnetic wave to be classical and weak enough to neglect any energy level shifts from the dynamic Stark effect.

In the frame rotating with an angular frequency Ω the energy level diagram looks as shown in figure 3.1b. As was shown in section 2.1, the light frequency in the rotating frame is shifted or split (depending on polarization). The eigenvalues of the Schrödinger equation in the rotating frame (equation 3.12) differ from those in the laboratory system because of the presence of the term $\Omega L'_z$. We call these eigenvalues pseudo-energy levels, because as Ω is high enough they may even be shifted below the ground state.

One can easily understand the pseudo-energy level shifts if one refers to the light frequency transformation in sec. 2.1: the resonant light in the laboratory frame has to remain resonant in the rotating frame, whatever the rotation fre-

quency Ω is. As the rotating frame is not coupled there is no observable frequency shift.

3.3 Three-level atom in the rotating frame

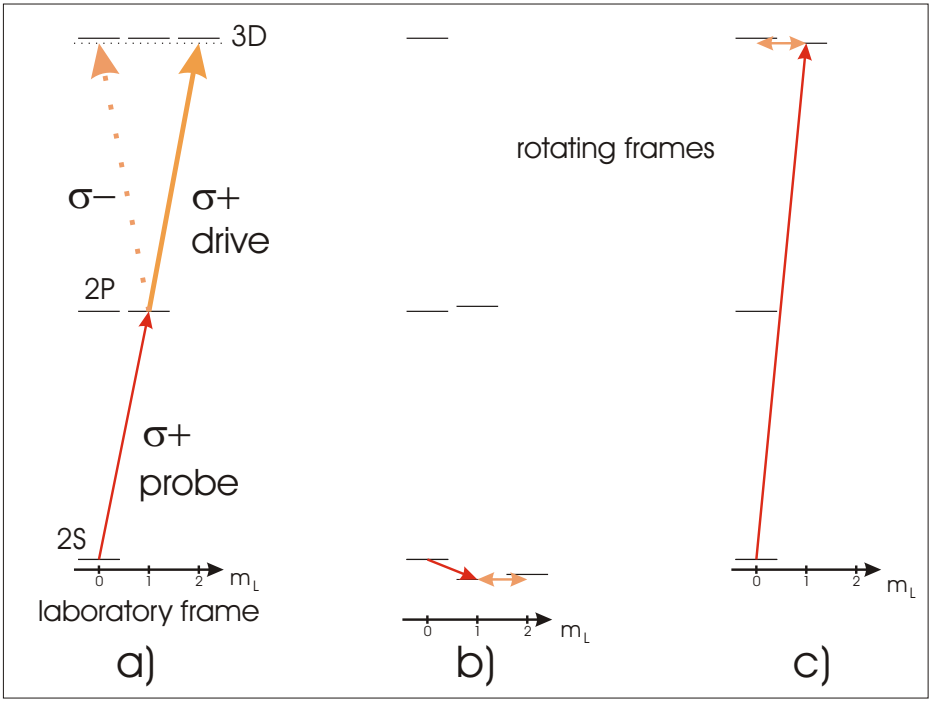

Figure 3.2: Three-level lithium atom considered in the laboratory and rotating frames.

A three-level atom in two light fields, as a theoretically and experimentally well investigated system, offers a good opportunity for exploring the rotational frequency shift and comparing it with the traditional analysis. Consider the three-level atom (inclusive m sub-levels) put in a probe (weak) and a drive (strong) circular polarized electromagnetic field. One can analyze this quantum system by referring traditionally to the dynamic Stark effect, or to the rotational frequency shift. The following considerations apply to the lithium atom, a good example for a three-level system, and to the experiments described in sec. 4.2.

3.3.1 Traditional view - Dynamic Stark Effect

The dynamic Stark shift arises from the virtual transitions between atomic levels caused by near-resonant light [10]. For circularly polarized light fields, the effect has been investigated and interpreted in terms of a *fictitious magnetic field* ([11], see also sec. 5.3). This idea was further developed in the explorations of the recently observed *Zeeman-like ac-Stark shift* [12, 13], the light-induced spin precession [14, 15], and the optical Stern-Gerlach effect [16].

The level diagram of the considered atom in the laboratory frame is shown in figure 3.2a. The probe field enables the investigation of the energy shift of the $|2P, m_L = 1\rangle$ level. The energy shift is caused by a strong driving field, which is tuned near the $|2P\rangle \rightarrow |3D\rangle$ transition. The dynamic Stark effect of the $\left|2P_{3/2}, m_L = 1\right\rangle$ level is [10]

$$\Delta E_{2P_{3/2}} = -\sum_f \frac{\langle f| \mu_\pm \left|2P_{3/2}, 1\right\rangle^2 \varepsilon^2}{E_f - E_{2P} - \hbar\Omega}, \tag{3.16}$$

where $\mu_\pm = -er\sin\theta(\sin\varphi \pm i\cos\varphi)$ is the dipole transition operator, and $\langle f| \mu_\pm \left|2P_{3/2}, 1\right\rangle$ is the matrix element between $|2P, m_L = 1\rangle$ and the final state $|f\rangle$. ε and Ω are the electric field strength and the angular frequency of the driving field, respectively. Due to the dominating resonance term in the denominator, equation 3.16 can be re-written as

$$\Delta E_{2P_{3/2}} \simeq -\sum \frac{\langle 3D| \mu_\pm \left|2P_{3/2}, 1\right\rangle^2 \varepsilon^2}{E_{3D} - E_{2P_{3/2}} - \hbar\Omega}, \tag{3.17}$$

where the summation is carried out over the fine-structure and m sub-levels, depending on the polarization of the light beam. When this is σ^+ (the same as the polarization of the probe beam), we obtain

$$\Delta E^+_{2P_{3/2}} \simeq -\frac{\left\langle 3D_{5/2}, 2\right| \mu_+ \left|2P_{3/2}, 1\right\rangle^2 \varepsilon^2}{E_{3D_{5/2}} - E_{2P_{3/2}} - \hbar\Omega}, \tag{3.18}$$

and for the case when the beams have opposite circular polarization

$$\Delta E^-_{2P_{3/2}} \simeq -\frac{\left\langle 3D_{5/2}, 0\right| \mu_- \left|2P_{3/2}, 1\right\rangle^2 \varepsilon^2}{E_{3D_{5/2}} - E_{2P_{3/2}} - \hbar\Omega} - \frac{\left\langle 3D_{3/2}, 0\right| \mu_- \left|2P_{3/2}, 1\right\rangle^2 \varepsilon^2}{E_{3D_{3/2}} - E_{2P_{3/2}} - \hbar\Omega}. \tag{3.19}$$

One can calculate the matrix elements explicitly [17] assuming the wave functions are approximately hydrogenic:

$$\left\langle 3D_{5/2}, 2\right| \mu_+ \left|2P_{3/2}, 1\right\rangle = -e\int_0^\infty R_{32}R_{21}r^3 dr \times$$

$$\times \int_0^\pi \sqrt{\frac{5}{\pi}}\sin^4\theta d\theta \int_0^{2\pi} d\varphi = \sqrt{\frac{45\pi}{16}}\mathbf{R}, \tag{3.20}$$

$$\left\langle 3D_{5/2},0\right|\mu_-\left|2P_{3/2},1\right\rangle = -e\int_0^\infty R_{32}R_{21}r^3dr\times$$

$$\times\int_0^\pi\sqrt{\frac{15}{2\pi}}\sin^2\theta(3\cos^2\theta-1)d\theta\int_0^{2\pi}d\varphi=\sqrt{\frac{15\pi}{32}}\mathbf{R}, \tag{3.21}$$

$$\left\langle 3D_{3/2},0\right|\mu_-\left|2P_{3/2},1\right\rangle = -e\int_0^\infty R_{32}R_{21}r^3dr\times$$

$$\times\int_0^\pi\sqrt{\frac{15}{2\pi}}\sin^2\theta(3\cos^2\theta-1)d\theta\int_0^{2\pi}d\varphi=\sqrt{\frac{15\pi}{32}}\mathbf{R}, \tag{3.22}$$

where $\mathbf{R}$ is the radial integral common for all above dipole moment matrix elements. Using equations 3.20, 3.21 and 3.22 in 3.18 and 3.19 we get

$$\Delta E^+_{2P_{3/2}}\simeq\frac{45\mathbf{R}^2\varepsilon^2}{16(E_{3D_{5/2}}-E_{2P_{3/2}}-\hbar\Omega)}, \tag{3.23}$$

and

$$\Delta E^-_{2P_{3/2}}\simeq\frac{15\mathbf{R}^2\varepsilon^2}{32(E_{3D_{5/2}}-E_{2P_{3/2}}-\hbar\Omega)}+\frac{15\mathbf{R}^2\varepsilon^2}{32(E_{3D_{3/2}}-E_{2P_{3/2}}-\hbar\Omega)}. \tag{3.24}$$

Assuming that the de-tunings of the Stark beam from the different fine structure sub-levels of $|3D\rangle$ are similar, one gets

$$\Delta E^-_{2P_{3/2}}\simeq\frac{15\mathbf{R}^2\varepsilon^2}{16(E_{3D_{5/2}}-E_{2P_{3/2}}-\hbar\Omega)}. \tag{3.25}$$

Comparing equations 3.25 and 3.23 gives the relation between the energy shifts caused by different drive beam polarizations

$$\frac{\Delta E^+_{2P_{3/2}}}{\Delta E^-_{2P_{3/2}}}\simeq 3 \tag{3.26}$$

for the same beam intensities and de-tunings.

3.3.2 Rotating frame approach

Consider now the three-level atom in the frame rotating with the angular frequency Ω, co-rotating with the driving field. The pseudo-energy level diagrams for the two kinds of circular polarization (rotation direction) are shown in the figures 3.2b and c.

In the case when the Stark beam is σ^+-polarized, see fig. 3.2b, the pseudo-energy levels $E'_{2P_{3/2,1}}=E_{2P_{3/2,m_L=1}}-\hbar\Omega$ and $E'_{3D_{5/2,2}}=E_{3D_{5/2,m_L=2}}-2\hbar\Omega$ lie

nearby each other, and the static field (in the rotating frame) is responsible for the static Stark effect. Let us write down the part of the hamiltonian matrix

$$H' = \begin{pmatrix} E_{3D_{5/2,2}} - 2\hbar\Omega & \varepsilon\mu^{+}_{5/2} \\ \varepsilon\mu^{+}_{5/2} & E_{2P_{3/2,1}} - \hbar\Omega \end{pmatrix}, \tag{3.27}$$

where

$$\mu^{+}_{5/2} = \langle 3D_{5/2}, 2 | \, \mu_{+} \, | 2P_{3/2}, 1 \rangle \tag{3.28}$$

is an electric dipole transition moment, and μ_{+} is the dipole moment operator. Rewriting the first diagonal term in 3.27 in terms of the de-tuning,

$$\delta_{5/2} = E_{3D_{5/2}} - E_{2P_{3/2}} - \hbar\Omega, \tag{3.29}$$

we get

$$H' = \begin{pmatrix} E_{2P_{3/2,1}} + \delta_{5/2} - \hbar\Omega & \varepsilon\mu^{+}_{5/2} \\ \varepsilon\mu^{+}_{5/2} & E_{2P_{3/2,1}} - \hbar\Omega \end{pmatrix}. \tag{3.30}$$

Solving for the eigenvalue we get

$$E'^{+}_{2P_{3/2,1}} = E_{2P_{3/2,1}} + \frac{\delta_{5/2}}{2} - \sqrt{(\varepsilon\mu^{+}_{5/2})^2 + \frac{\delta^2_{5/2}}{4}} - \hbar\Omega. \tag{3.31}$$

Assuming $\varepsilon\mu^{+}_{5/2} \ll \delta_{5/2}$, we get

$$E'^{+}_{2P_{3/2,1}} \simeq E_{2P_{3/2,1}} - \frac{(\varepsilon\mu^{+}_{5/2})^2}{\delta_{5/2}} - \hbar\Omega. \tag{3.32}$$

Now we want to calculate the influence of the field effect on spectroscopic transitions in the laboratory frame. Let us consider the transition between the $|2S\rangle$ ground state and $|2P_{3/2,1}\rangle$ state. In the rotating frame we have the transition frequency

$$h\nu'^{+} = E'^{+}_{2P_{3/2,1}} - E'_{2S}, \tag{3.33}$$

where $E'_{2S} = E_{2S} = 0$ is the energy of the ground state possessing no angular momentum. Transforming the frequency ν'^{+} back to the laboratory frame, we get

$$h\nu^{+} = h\nu'^{+} + \hbar\Omega, \tag{3.34}$$

and the frequency shift caused by the rotating field is $\Delta\nu^{+} = \nu^{+} - \nu$ where ν is the transition frequency when no external field is applied. Then the energy shift becomes

$$h\Delta\nu^{+} = \Delta E^{+}_{2P_{3/2}} = E'^{+}_{2P_{3/2,1}} - E_{2P_{3/2,1}} + \hbar\Omega \simeq -\frac{(\varepsilon\mu^{+}_{5/2})^2}{\delta_{5/2}} \tag{3.35}$$

which is the result of eq. 3.18.

In the case when the Stark beam polarization is σ^-, the relevant part of the hamiltonian H' in the frame rotating in the direction opposite to the previous case looks

$$H' = \begin{pmatrix} E_{3D_{5/2,0}} - 2\hbar\Omega & 0 & \varepsilon\mu^-_{5/2} \\ 0 & E_{3D_{3/2,0}} - 2\hbar\Omega & \varepsilon\mu^-_{3/2} \\ \varepsilon\mu^-_{5/2} & \varepsilon\mu^-_{3/2} & E_{2P_{3/2,1}} - \hbar\Omega \end{pmatrix}. \tag{3.36}$$

Introducing

$$\delta_{3/2} = E_{3D_{3/2}} - E_{2P_{3/2}} - \hbar\Omega \tag{3.37}$$

and $\delta_{5/2}$ we get

$$H' = \begin{pmatrix} E_{2P_{3/2,1}} + \delta_{5/2} - \hbar\Omega & 0 & \varepsilon\mu^-_{5/2} \\ 0 & E_{2P_{3/2,1}} + \delta_{3/2} - \hbar\Omega & \varepsilon\mu^-_{3/2} \\ \varepsilon\mu^-_{5/2} & \varepsilon\mu^-_{3/2} & E_{2P_{3/2,1}} - \hbar\Omega \end{pmatrix}. \tag{3.38}$$

Assuming similar de-tunings: $\delta_{5/2} \simeq \delta_{3/2} = \delta$, $\varepsilon\mu^-_{5/2} \ll \delta_{5/2}$ and $\varepsilon\mu^-_{3/2} \ll \delta_{5/2}$ we obtain

$$E'^-_{2P_{3/2,1}} \simeq E_{2P_{3/2,1}} - \frac{(\varepsilon\mu^-_{5/2})^2}{\delta} - \frac{(\varepsilon\mu^-_{3/2})^2}{\delta} - \hbar\Omega, \tag{3.39}$$

and the energy shift becomes

$$\Delta E^-_{2P_{3/2}} = E'^-_{2P_{3/2,1}} - E_{2P_{3/2,1}} + \hbar\Omega \simeq -\frac{(\varepsilon\mu^-_{5/2})^2}{\delta} - \frac{(\varepsilon\mu^-_{3/2})^2}{\delta} \tag{3.40}$$

which is the same as eq. 3.19.

Thus, as expected, calculations performed in the RFS framework give the predictions for the observables in agreement with the dynamic Stark effect approach. The advantage of the RFS procedure in this case is the possibility of considering the Stark effect as a static one.

3.4 Theory of the intermediate RFS in a molecular system

This section refers to the experiments to be described in sec. 4.3. The optical transition 3_{31} $4^1\tilde{A}$ $^1A_2 \leftarrow 2_{20}$ $0^0\tilde{X}$ $^1A_1$ of the thioformaldehyde molecule at 16808.71 cm^{-1} (595 nm) was chosen for the following reasons:

- the transition lies in a convenient rhodamine 6G dye wavelength region,
- the transition is relatively strong,

- the rotational quantum numbers are small for an easy comparison with theory,
- they are, however, big enough to treat the molecule like a symmetric top which in turn means that the Stark effect can be considered linear [20],
- there are no optical transitions in the neighborhood.

The static Stark effect of the $3_{31} \leftarrow 2_{20}$ transition has been investigated by FUNG and RAMSAY [20]. The electric dipole moments of the electronic ground and excited states are $\mu_g = 1.6491(4)$ Debye[1] [22] and $\mu_e = 0.815(20)$ D [20], respectively. The experimental conditions allow it to investigate the intermediate RFS, meaning that $\hbar\Omega \simeq \mu\varepsilon$. The electric field strengths for the condition

$$\hbar\Omega = \mu_{g,e}\varepsilon_{g,e} \tag{3.41}$$

are

$$\begin{aligned} \varepsilon_g &= 9.7\ \mathrm{V/mm} \\ \varepsilon_e &= 19.7\ \mathrm{V/mm}. \end{aligned} \tag{3.42}$$

The hamiltonian of the free molecule subject to an electrical field rotating in the XY laboratory plane is

$$H_{g,e} = H_0 - \varepsilon\mu_{g,e}(\Phi_{Yz}\cos\Omega t + \Phi_{Xz}\sin\Omega t), \tag{3.43}$$

where Φ_{Xz} and Φ_{Yz} are direction cosines of the axis of molecular z with reference to the space-fixed X and Y axes, respectively [21]. In the frame co-rotating with the field we have

$$H'_{g,e} = H_0 - \varepsilon\mu_{g,e}\Phi_{Yz} + \hbar\Omega P_Z, \tag{3.44}$$

where the last term arises from the transformation to the rotating frame, and P_Z is the angular momentum component operator along the rotation axis. So the diagonal matrix elements of the hamiltonian are of the form $n\hbar\Omega$, and the off-diagonal ones can be calculated using eq. 10.3 and table 2.1 from GORDY & COOK [21]. One obtains the hamiltonian explicitly in the m_J-base for the $J = 2, K = 2$ state:

$$H'_{22} = H_0 + \begin{pmatrix} 2\hbar\Omega & \frac{\sqrt{4}}{6}\mu_g\varepsilon & 0 & 0 & 0 \\ \frac{\sqrt{4}}{6}\mu_g\varepsilon & \hbar\Omega & \frac{\sqrt{6}}{6}\mu_g\varepsilon & 0 & 0 \\ 0 & \frac{\sqrt{6}}{6}\mu_g\varepsilon & 0 & \frac{\sqrt{6}}{6}\mu_g\varepsilon & 0 \\ 0 & 0 & \frac{\sqrt{6}}{6}\mu_g\varepsilon & -\hbar\Omega & \frac{\sqrt{4}}{6}\mu_g\varepsilon \\ 0 & 0 & 0 & \frac{\sqrt{4}}{6}\mu_g\varepsilon & -2\hbar\Omega \end{pmatrix} \tag{3.45}$$

[1] 1 Debye = 1 D = 3.33564110^{-30} Cm

and for the $J = 3, K = 3$ state:

$$H'_{33} = H_0 + \begin{pmatrix} 3\hbar\Omega & \frac{\sqrt{6}}{8}\mu_e\varepsilon & 0 & 0 & 0 & 0 & 0 \\ \frac{\sqrt{6}}{8}\mu_e\varepsilon & 2\hbar\Omega & \frac{\sqrt{10}}{8}\mu_e\varepsilon & 0 & 0 & 0 & 0 \\ 0 & \frac{\sqrt{10}}{8}\mu_e\varepsilon & \hbar\Omega & \frac{\sqrt{12}}{8}\mu_e\varepsilon & 0 & 0 & 0 \\ 0 & 0 & \frac{\sqrt{12}}{8}\mu_e\varepsilon & 0 & \frac{\sqrt{12}}{8}\mu_e\varepsilon & 0 & 0 \\ 0 & 0 & 0 & \frac{\sqrt{12}}{8}\mu_e\varepsilon & -\hbar\Omega & \frac{\sqrt{10}}{8}\mu_e\varepsilon & 0 \\ 0 & 0 & 0 & 0 & \frac{\sqrt{10}}{8}\mu_e\varepsilon & -2\hbar\Omega & \frac{\sqrt{6}}{8}\mu_e\varepsilon \\ 0 & 0 & 0 & 0 & 0 & \frac{\sqrt{6}}{8}\mu_e\varepsilon & -3\hbar\Omega \end{pmatrix} \tag{3.46}$$

As the Hamilton operators above are time independent, one can solve the static eigenvalue problem. The eigenvalues are

$$\Delta E_{22} = 0, \pm\sqrt{\frac{{\mu_g}^2\varepsilon^2}{9} + \hbar^2\Omega^2}, \pm\sqrt{\frac{4{\mu_g}^2\varepsilon^2}{9} + 4\hbar^2\Omega^2} \tag{3.47}$$

for the 2_{20} state, and

$$\Delta E_{33} = 0, \pm\sqrt{\frac{{\mu_e}^2\varepsilon^2}{16} + \hbar^2\Omega^2}, \pm\sqrt{\frac{4{\mu_e}^2\varepsilon^2}{16} + 4\hbar^2\Omega^2}, \pm\sqrt{\frac{9{\mu_e}^2\varepsilon^2}{16} + 9\hbar^2\Omega^2} \tag{3.48}$$

for the 3_{31} state. The transition frequencies for the circularly polarized light ($\Delta m = +1$ selection rule) are

$$\begin{aligned} \nu_{3\leftarrow 2} &= \nu_0 + \frac{1}{h}\left(\sqrt{\frac{9{\mu_e}^2\varepsilon^2}{16} + 9\hbar^2\Omega^2} - \sqrt{\frac{4{\mu_g}^2\varepsilon^2}{9} + 4\hbar^2\Omega^2} - \hbar\Omega\right), \\ \nu_{2\leftarrow 1} &= \nu_0 + \frac{1}{h}\left(\sqrt{\frac{4{\mu_e}^2\varepsilon^2}{16} + 4\hbar^2\Omega^2} - \sqrt{\frac{{\mu_g}^2\varepsilon^2}{9} + \hbar^2\Omega^2} - \hbar\Omega\right), \\ \nu_{1\leftarrow 0} &= \nu_0 + \frac{1}{h}\left(\sqrt{\frac{{\mu_e}^2\varepsilon^2}{16} + \hbar^2\Omega^2} - \hbar\Omega\right), \\ \nu_{0\leftarrow -1} &= \nu_0 + \frac{1}{h}\left(\sqrt{\frac{{\mu_g}^2\varepsilon^2}{9} + \hbar^2\Omega^2} - \hbar\Omega\right), \\ \nu_{-1\leftarrow -2} &= \nu_0 + \frac{1}{h}\left(-\sqrt{\frac{{\mu_e}^2\varepsilon^2}{16} + \hbar^2\Omega^2} + \sqrt{\frac{4{\mu_g}^2\varepsilon^2}{9} + 4\hbar^2\Omega^2} - \hbar\Omega\right) \end{aligned} \tag{3.49}$$

where the $\hbar\Omega$ term is due to the transformation of the light frequency back to the laboratory frame, and ν_0 is the frequency of the $3_{31} \leftarrow 2_{20}$ transition observed without any external field. For the $\Delta m = -1$ selection rule we have

$$\nu_{-3\leftarrow -2} = \nu_0 + \frac{1}{h}\left(-\sqrt{\frac{9{\mu_e}^2\varepsilon^2}{16} + 9\hbar^2\Omega^2} + \sqrt{\frac{4{\mu_g}^2\varepsilon^2}{9} + 4\hbar^2\Omega^2} + \hbar\Omega\right),$$

$$
\begin{aligned}
\nu_{-2\leftarrow -1} &= \nu_0 + \frac{1}{h}\left(-\sqrt{\frac{4{\mu_e}^2\varepsilon^2}{16} + 4\hbar^2\Omega^2} + \sqrt{\frac{{\mu_g}^2\varepsilon^2}{9} + \hbar^2\Omega^2} + \hbar\Omega\right), \\
\nu_{-1\leftarrow 0} &= \nu_0 + \frac{1}{h}\left(\sqrt{\frac{{\mu_e}^2\varepsilon^2}{16} + \hbar^2\Omega^2} + \hbar\Omega\right), \\
\nu_{0\leftarrow 1} &= \nu_0 + \frac{1}{h}\left(-\sqrt{\frac{{\mu_g}^2\varepsilon^2}{9} + \hbar^2\Omega^2} + \hbar\Omega\right), \\
\nu_{1\leftarrow 2} &= \nu_0 + \frac{1}{h}\left(\sqrt{\frac{{\mu_e}^2\varepsilon^2}{16} + \hbar^2\Omega^2} - \sqrt{\frac{4{\mu_g}^2\varepsilon^2}{9} + 4\hbar^2\Omega^2} + \hbar\Omega\right). \qquad (3.50)
\end{aligned}
$$

Note that the sign of the $\hbar\Omega$ term is now opposite to that in eqs. 3.49. The $\Delta m = \pm 1$ selection rules dominate as long as $\hbar\Omega$ is larger than the coupling energy. With increasing electric field amplitude additional transitions become probable.

Chapter 4

Experimental

'Quantum phenomena do not occur in Hilbert space; they occur in a laboratory. If you visit a real laboratory, you will never find Hermitian operators there.' A. Peres and D. A. Terno [18]

4.1 Laser spectroscopic means

The laser-system used in this work consists of a Spectra Physics 2045E argon-ion pump laser and two Spectra Physics 380D continuous wave dye ring lasers. The dye lasers can be used simultaneously where they deliver visible light of powers between 100 and 600 mW, depending on wavelength and dye. The bandwidth of about 300 kHz meets the requirements for sub-doppler spectroscopy [19]. Faraday effect optical diodes from Gsänger were put directly behind the dye lasers to avoid back-reflected beams affecting the laser operation. The direction of the linear polarization can be controlled by adjustable polarization rotators ($\lambda/2$ Fresnel rhombs). The wavenumber (or wavelength) of the laser light was measured with a Burleigh digital wavemeter, with an accuracy of about 0.03 cm^{-1} or 1 GHz. Photomultiplier tube modules (PMTs) from Seefelder Messtechnik were used for a sensitive detection of the fluorescence light. The PMT modules consist of preamplifiers of rise/fall times of about 30 μs, and broadband photomultiplier tubes from Hamamatsu, models R928 and R955.

4.2 Fast rotation RFS in atomic lithium

4.2.1 Apparatus

The experimental setup is shown in figure 4.1. Two dye lasers work with the dyes DCM and rhodamine 6G, respectively. Red light from the DCM dye laser, tuned to a wavelength of about 14904 cm^{-1} or 670 nm where the transition

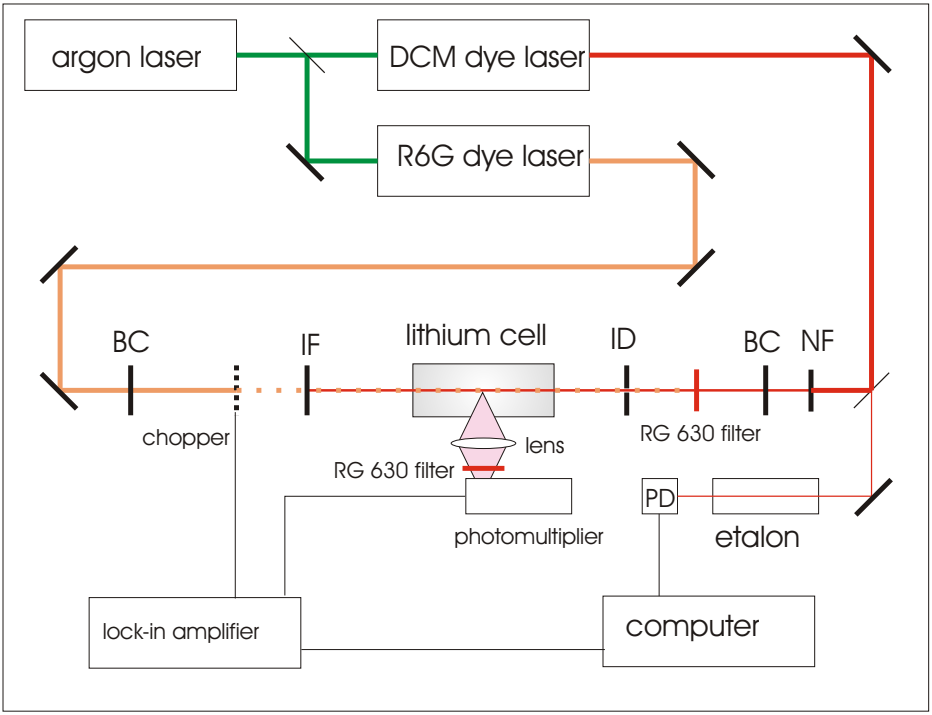

Figure 4.1: Experimental setup. BC - Babinet-Soleil compensator, ID - iris diaphragm, NF - neutral density filter, PD - photodiode, IF -interference filter, high reflection at 670 nm and high transmission at 610 nm. The chopped drive beam is indicated by dots.

$|2P\rangle \leftarrow |2S\rangle$ takes place in lithium, is guided back and forth through the lithium-vapor cell. It is reflected back by an interference filter which has a high reflection near 670 nm, and a high transmission near 610 nm. Unidirectional orange light, produced by the rhodamine 6G laser, enters the cell via the same path. A high-temperature cell constructed by Otto [23, 24] has been used. Lithium was heated in the melting-pot inside the cell to about 200°C. Under this condition, the number density is appropriate for carrying out saturation spectroscopy in the vapor phase. The anti-reflex coated glass windows were oriented perpendicularly to the laser beam in order to not affect the light's polarization. The fluorescence from the transition $|2S\rangle \leftarrow |2P\rangle$ is detected by a photomultiplier tube, PMT, at about 670 nm. In order to remove the strong orange stray-light from the drive (Stark) beam, a color-glass long-pass filter RG 630 was put in front of the PMT. The drive light beam was modulated by a chopper at frequency of about 1.5 kHz, and the spectra were recorded with the aid of a lock-in amplifier. The

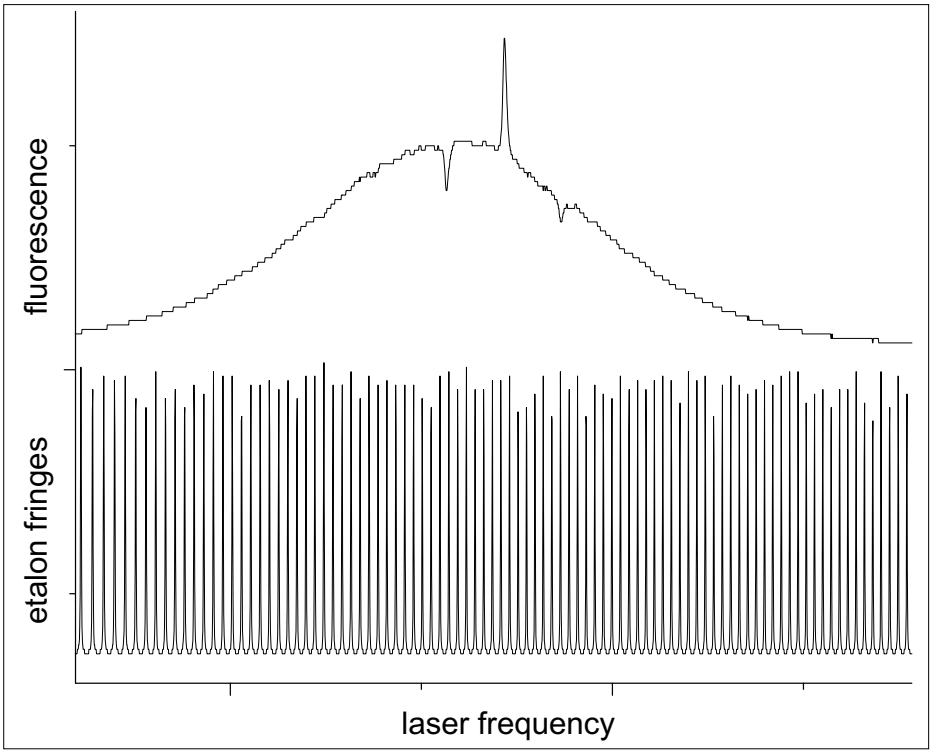

Figure 4.2: The $\left|2P_{3/2}\right\rangle \leftarrow \left|2S_{1/2}\right\rangle$ saturation spectrum of lithium. The *Lamb dips* on either side of the cross-over peak are due to the hyperfine splitting of the $\left|2S_{1/2}\right\rangle$ level. Here and in the following the difference of two etalon transmission peaks (below, simultaneously recorded) is 61.0479 MHz.

light beams were not focussed. An iris diaphragm was used to keep the diameter of the probe beam smaller than that of the drive beam. In this way, the drive beam intensity could be held constant in the probe beam volume. The power of the drive beam was about 220 mW. The probe beam has been attenuated to about 1 mW with the aid of a neutral density filter in order to avoid saturation broadening of the *Lamb dips* [19]. The polarization of both light beams was carefully controlled by two Babinet-Soleil compensators [33], see appendix A.2. Part of the light was guided through an etalon showing a free spectral range (FSR) of 61.0479(88) MHz [24]. The red probe light was tuned to the transition $\left|2P_{3/2}\right\rangle \leftarrow \left|2S_{1/2}\right\rangle$ near 14904.00 cm^{-1}.

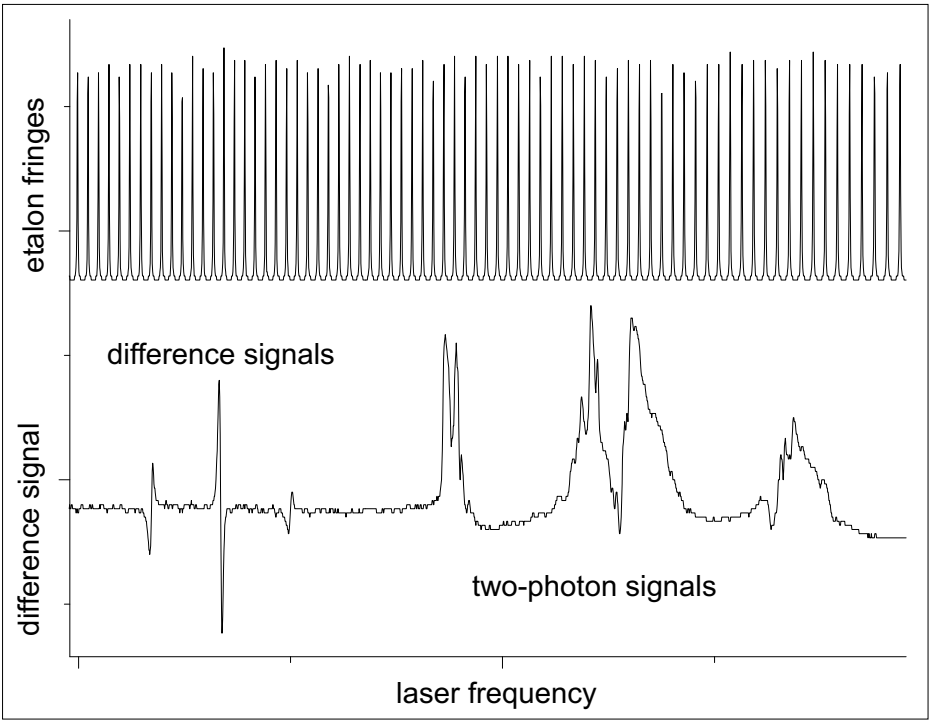

Figure 4.3: Stark effect modulated spectrum of the $|3D\rangle \leftarrow |2P\rangle$ transition of lithium for the linear drive beam polarization. The scan parameters were: lock-in sensitivity 3 mV, lock-in time constant 100 ms, PMT voltage 250 V, chopper frequency 1.5 kHz.

4.2.2 Results

A typical saturation spectrum, recorded with the chopped probe beam in absence of the drive beam, is shown in figure 4.2.

There are two *Lamb dips* inside the Doppler-profile which are caused by the hyperfine splitting of the ground state. The peak between them is the *cross-over* signal [19]. The spectral linewidth of the saturation signals amounts to about 25 MHz, which corresponds to the radiative lifetime of the $|2P\rangle$ state of lithium [25]. When the drive beam, slightly de-tuned from the transition $|3D\rangle \leftarrow |2P\rangle$, is modulated by the optical chopper, the intensity difference between fluorescences from the shifted and unshifted $|2P\rangle$ levels is observed. Figure 4.3 shows such an effect-modulated spectrum. The four structured signals at right are the two-photon signals from the transition $|3D\rangle \leftarrow |2S\rangle$. They show hyperfine structure of the $|2S\rangle$ and fine structure of the $|3D\rangle$ state, and appear when the sum of the laser light frequencies times h is equal to the energy difference between the

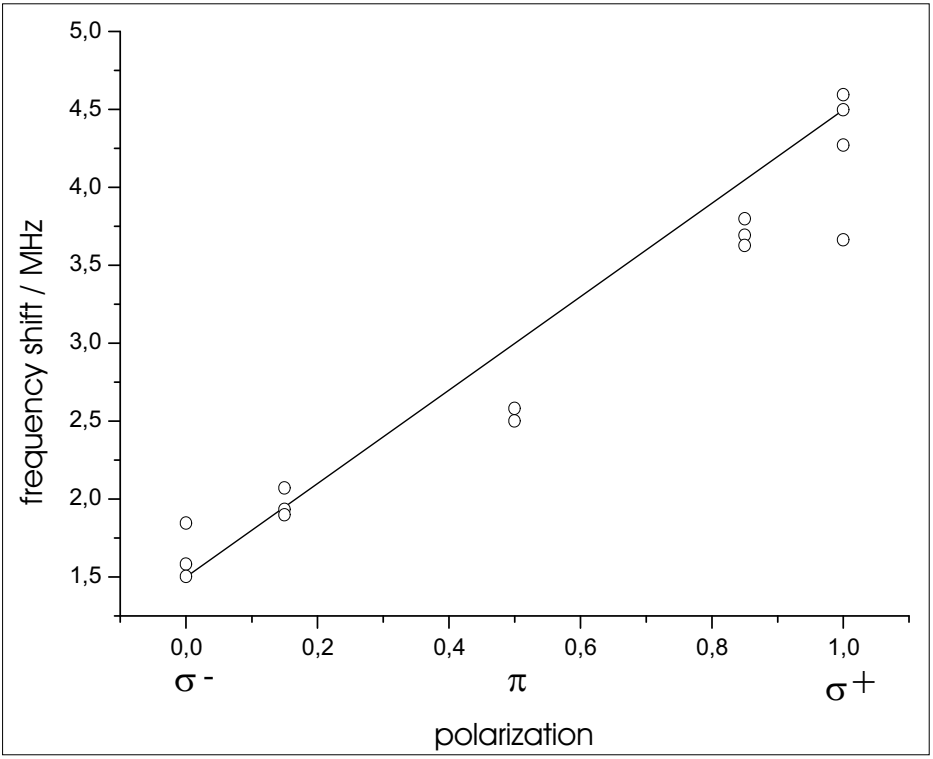

Figure 4.4: Frequency shift vs. Stark beam polarization. 0 on the horizontal axis means σ^- polarization, 0.5 linear and 1 σ^+ polarization. The errors of the frequency shifts are about 0.5 MHz. The solid line is calculated with the electric field strength of the drive beam fitted to the measured frequency shifts. The probe beam was always σ^+ polarized.

$|3D\rangle$ and $|2S\rangle$ states. The interferometer transmission signal (etalon fringes) was recorded simultaneously. It was used to control the de-tuning of the Stark beam by measuring the frequency distance between the effect-modulation and the two-photon signals. The evaluation of the frequency shifts of the $|2P\rangle$ state is described in detail in appendix A.1. The frequency shift caused by the drive beam was found to be about 1.5 MHz when the probe and the drive light polarizations were chosen oppositely, and 4.5 MHz when they were the same. Figure 4.4 shows the results for circular as well as linear and some elliptical polarizations of the drive beam. The relation of the two frequency shifts, $\Delta E^+_{2P_{3/2}}/\Delta E^-_{2P_{3/2}} \simeq 3$, is in agreement with theory, eq. 3.26.

4.3 Intermediate RFS in H_2CS molecules

4.3.1 Some properties of thioformaldehyde

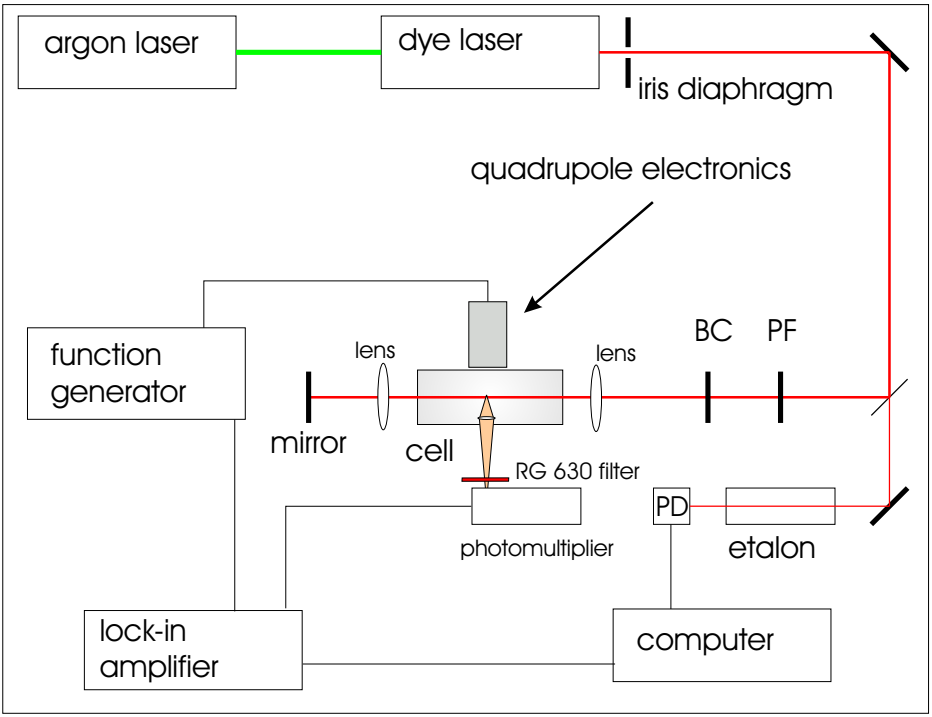

Figure 4.5: Arrangement for the saturation experiments with thioformaldehyde. The vacuum connections and the H_2CS production oven are not shown. BC - Babinet-Soleil compensator, PF - polarization filter, PD - photodiode.

Thioformaldehyde, H_2CS, is a spectroscopically well investigated molecule. The rotational and centrifugal distortion constants of H_2CS are known for the vibronic ground- and some excited states. The transition from the $0^0\tilde{X}\ ^1A_1$ ground state to the manifold of the first excited electronic state $4^1\tilde{A}\ ^1A_2$ lies in the convenient rhodamine 6G dye wavelength region. A disadvantage is that the molecule is not chemically stable - it polymerizes and must therefore be produced *in situ*. Thioformaldehyde is produced by the pyrolysis of trimethylene sulfide at about 860°C,

$$(CH_2)_3S \xrightarrow{860^\circ C} H_2CS + (CH_2)_2. \tag{4.1}$$

This is done by letting the trimethylene sulfide vapor flow through a heated fused silica pipe, and pumping on the pyrolysis products at the outlet of the observation

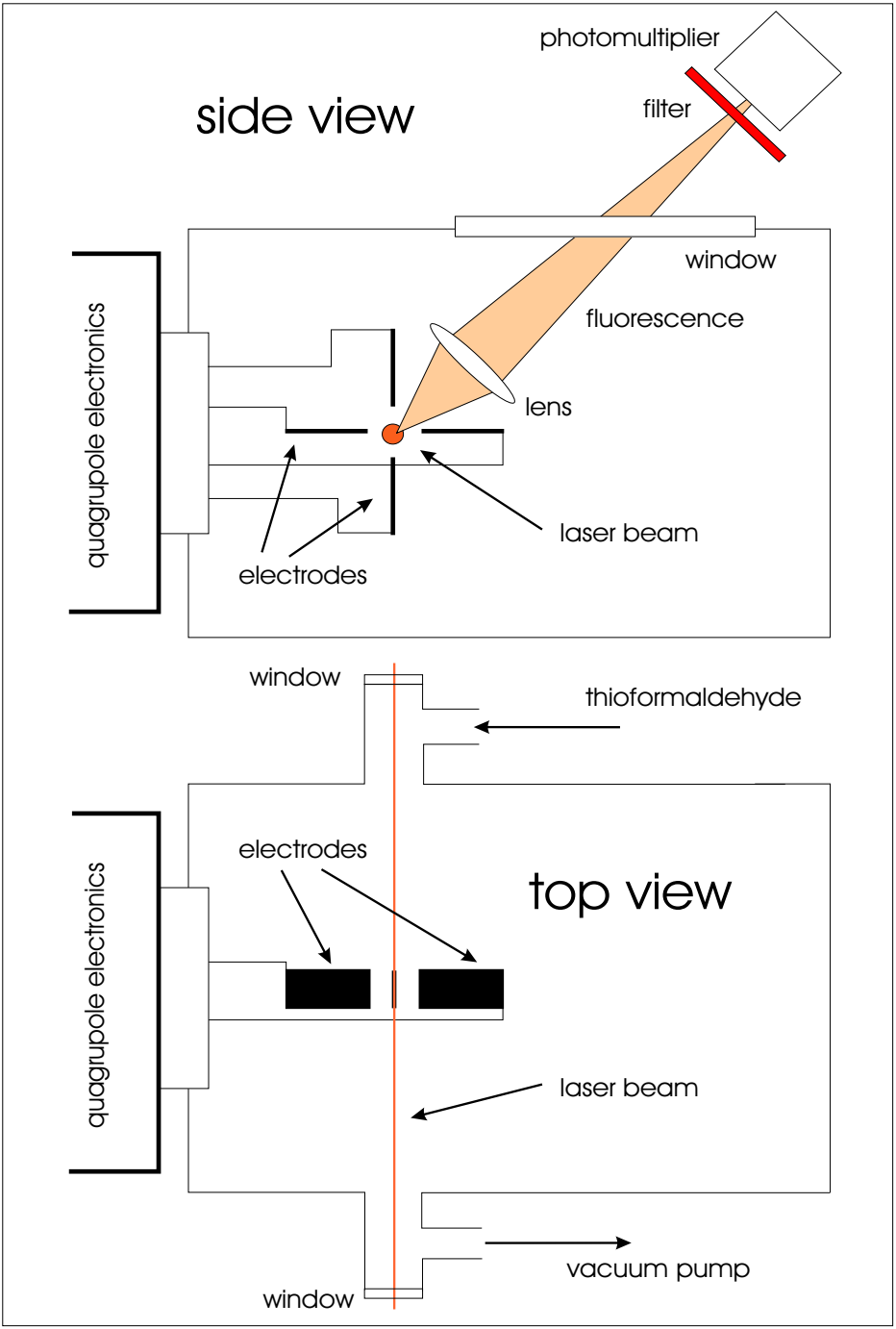

Figure 4.6: Details of the quadrupole setup for the thioformaldehyde experiments, compare the photograph in fig. 4.7.

cell. The liquid nitrogen cooled vapor trap has to be placed directly in front of the vacuum pump in order to protect it from the sulfur compounds.

4.3.2 Apparatus

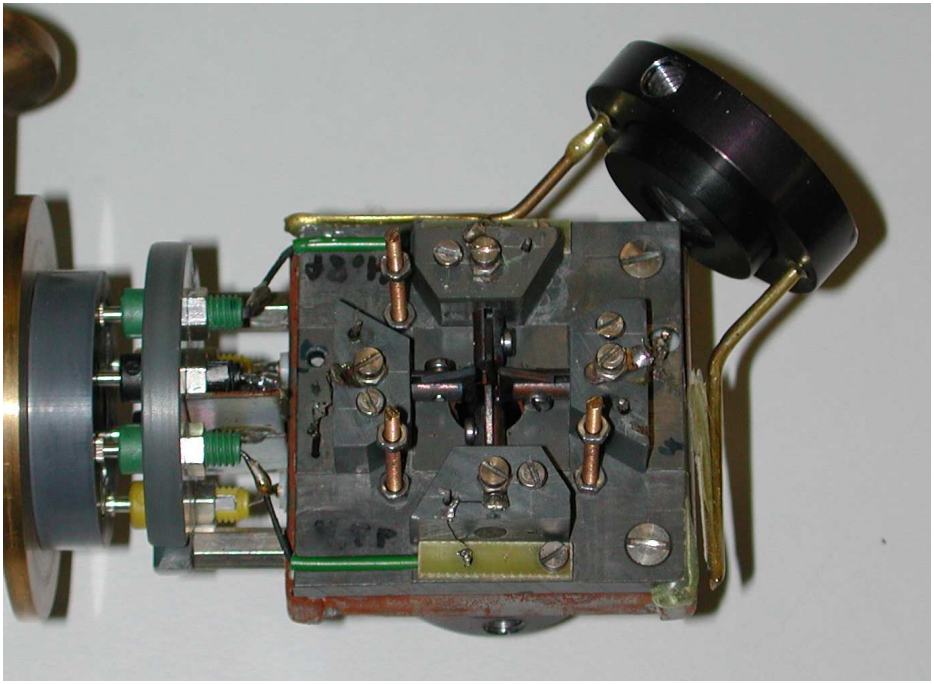

Figure 4.7: Photograph of the quadrupole as schematically explained in fig. 4.6. The beam-centering iris diaphragm is removed.

The experimental setup is shown in figures 4.5 and 4.6. The laser beam was guided through the cell back and forth and focussed in the center to a diameter of about 20 μm in order to achieve enough power density for the saturation spectroscopy. The focal length of the focussing lenses was 150 mm. The lenses as well as the cell windows were anti-reflex coated in order to reduce the stray-light. The cell windows were oriented perpendicular to the beam in order to not affect the light polarization. The electrical field, rotating with the constant frequency of 80.63 MHz, was generated by a quadrupole setup of electrodes. The device was made of 1 mm thick copper plates, and the distance between the opposite electrodes was 3.0 mm. Two iris diaphragms were fastened on two sides of the quadrupole holder (they are not shown in the figures). In order to adjust the distance between the electrodes and to ensure they are parallel a 3.0 mm

Table 4.1: Repeated observed frequency shifts (in MHz). Sense of circular polarization conform with the field rotation. The measurement error is estimated to be about 1 MHz. The error of the mean value is the standard deviation in units of the last significant digit. The errors of the theoretical values are due to the 5 % uncertainty of the electrical field amplitude.

transition	$3 \leftarrow 2$	$2 \leftarrow 1$	$0 \leftarrow -1$	$-1 \leftarrow -2$	not assigned
field strength 22.5 V/mm	-28.4	-14.2	22.7	44.3	
	-29.2	-13.3	21.2	35.1	
	-29.0	-12.0	20.3	33.5	
	-34.7	-15.4	20.8	37.7	
	-30.5	-13.1	19.6	37.0	
mean value	-30.4(26)	-13.6(13)	20.9(12)	37.5(41)	
theory	-32.8(16)	-14.8(7)	21.2(11)	39.3(20)	
field strength 26.3 V/mm	-41.2	-15.6	26.1	45.4	
	-38.2	-15.9			
	-45.5	-20.5	29.9		
	-38.4	-19.2	22.7	43.1	
mean value	-40.8(34)	-17.8(24)	26.2(36)	44.3(17)	
theory	-42.8(21)	-19.2(10)	28.0(14)	51.6(26)	
field strength 30.0 V/mm	-56.5	-26.2	38.6	70.8	
	-48.6	-22.2	34.0	62.4	
	-56.8	-23.7	39.7	72.7	104.6
	-48.6	-17.4	38.6	63.7	
	-53.6	-23.8	35.1	65.6	93.7, 121.6
mean value	-52.8(41)	-22.7(32)	37.2(25)	67.0(45)	
theory	-53.2(27)	-23.8(12)	35.1(18)	64.5(32)	

diameter metal rod was placed between them, and the electrodes were arranged to contact the rod. After this adjustment the diameters of the iris diaphragms were reduced to about 1 mm in order to guarantee that the laser beam finds its way through the center of the quadrupole and is oriented parallel to the field rotation axis. The whole experimental setup was put 5 m away from the laser so the back beam path could be adjusted to cover the forward beam exactly enough for observing saturation dips. The beams were focussed. The power of the laser radiation was about 350 mW. The fluorescence was observed perpendicular to the laser beam. In order to collect as much fluorescence light as possible, a lens with a focal length of 20 mm was mounted close to the quadrupole, inside the vacuum chamber (see figs. 4.6 and 4.7). The broadband florescence from the electronically excited, vibronic ground band $0^0\tilde{A}\ ^1A_2$ to the electronic ground state manifold $0^0\tilde{X}\ ^1A_1$ was observed, and the laser stray-light was filtered out by a RG 630 long-pass color glass filter. The fluorescence light was detected

Table 4.2: Repeated observed frequency shifts (in MHz). Sense of circular polarization opposite to the field rotation. The measurement error is estimated to be about 1 MHz. The error of the mean value is the standard deviation in units of the last significant digit. The errors of the theoretical values are due to the 5 % uncertainty of the electrical field amplitude.

transition	$1 \leftarrow 2$	$0 \leftarrow 1$	$-2 \leftarrow -1$	$-3 \leftarrow -2$	not assigned
field strength 22.5 V/mm	-37.9 -43.7 -33.4 -48.1	-20.3 -24.3 -18.9 -22.6	13.0 12.2 11.6 17.0	31.2 32.1 27.7 38.6	
mean value	-40.8(64)	-21.5(24)	13.4(24)	32.4(45)	
theory	-39.3(20)	-21.2(11)	14.8(7)	32.8(16)	
field strength 26.3 V/mm		-28.3	17.9	41.7	
theory	-51.6(26)	-28.0(14)	19.2(10)	42.8(21)	
field strength 30.0 V/mm	-57.9 -62.9 -61.1 -64.0	-30.5 -34.4 -33.4 -38.6	19.8 23.8 23.3 21.3	44.6 53.6 50.1 49.7	-84.9 -93.2 -88.4 -88.7
mean value	-61.4(27)	-34.2(33)	22.0(18)	49.5(37)	-88.8(34)
theory	-64.5(32)	-35.1(18)	23.8(12)	53.2(27)	

with a photomultiplier. The signals were recorded via a lock-in amplifier using effect modulation. For that the rotating electric field was amplitude modulated (switched on and off) with a frequency of about 10 kHz.

4.3.3 Results

The phase of the lock-in demodulator has been chosen such that the difference between the two signals, fluorescence with and without the presence of the rotating field, was recorded. As the Doppler background profiles are very similar in both cases, they cancel out, and only sub-doppler signals remain in the observed spectra. The linewidth of the sub-doppler signals (*Lamb dips*) achieved was approximately 5 MHz. A typical scan is shown in figure 4.8. The peak is the inverted zero-field *Lamb dip*, and the two dips on either side are the signals observed with the rotating field in action. The fifth expected dip is not resolved because it is overlapped by the zero-field line. this causes one of the zero-field peak shoulders to be sharper than the other. The rotational frequency shifts of this system manifest themselves qualitatively in the following way:

- observed transition patterns are asymmetric with respect to the central peak, which is clearly seen in fig. 4.8 and tables 4.1 and 4.2,

- the frequency asymmetry in the $\Delta m = \pm 1$ selection rules along the rotation axis for the optical transitions caused by circular polarized radiation became present. If the electric Stark field perpendicular to the light beam direction would not rotate, there was no difference between the spectra obtained with the σ^+ and σ^- polarizations,

- the dependence of the Stark splitting on the electric field strength is not linear, see fig. 4.9, in contrast to the static linear case [20].

The results are collected in tables 4.1 and 4.2 and plotted in figure 4.9. The measurement error of the transition frequencies is estimated to be about 1 MHz. The unassigned transitions for the highest field strength available could be due to the transitions with the selection rules other than $\Delta m = \pm 1$, see sec. 3.4. The exact calculation of the transition probabilities have not been performed, an estimation shows that any 'forbidden' transition intensity would be at most 5% of a typical 'allowed' one for the maximal available field strength of 30 V/mm. The experimental results are compared with the theoretical values calculated from eqs. 3.49 and 3.50 in tables 4.1 and 4.2 and found to agree with the theory.

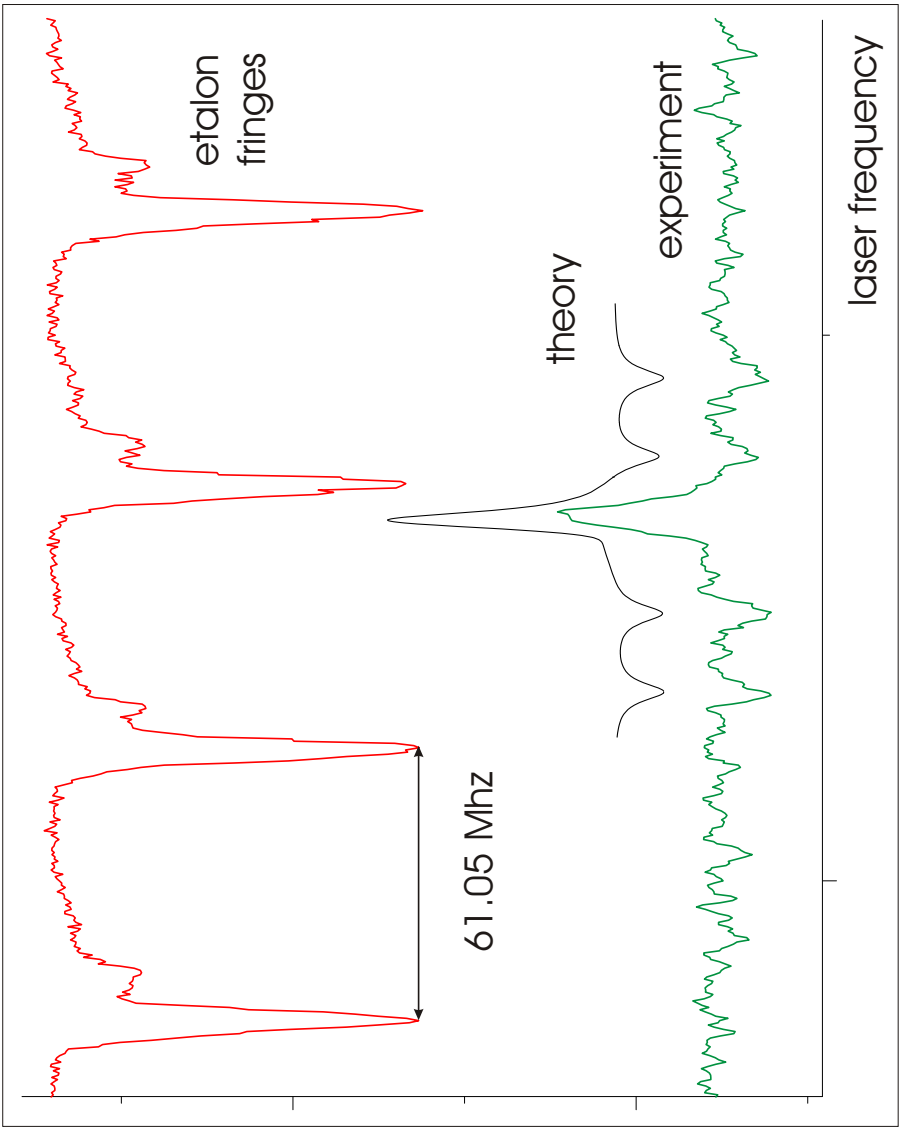

Figure 4.8: Scan of the saturated optical transition $3_{31}\ 4^1\tilde{A}\ ^1A_2 \leftarrow 2_{20}\ 0^0\tilde{X}\ ^1A_1$ of H_2CS in a rotating, AM modulated, electric field (green line). A simulated theoretical shape (black line) is shown on top of the measured signal. The interferometer transmission signal (etalon fringes) was recorded simultaneously. Scan parameters are: rotational frequency 80.63 MHz, electric field amplitude 22.5 V/mm, wavenumber of the central peak 16808.71 cm^{-1}, lock-in time constant 1 s, lock-in sensitivity 3 mV, PMT voltage 780 V, laser power 320 mW, thioformaldehyde pressure $3 \cdot 10^{-2}$ mbar.

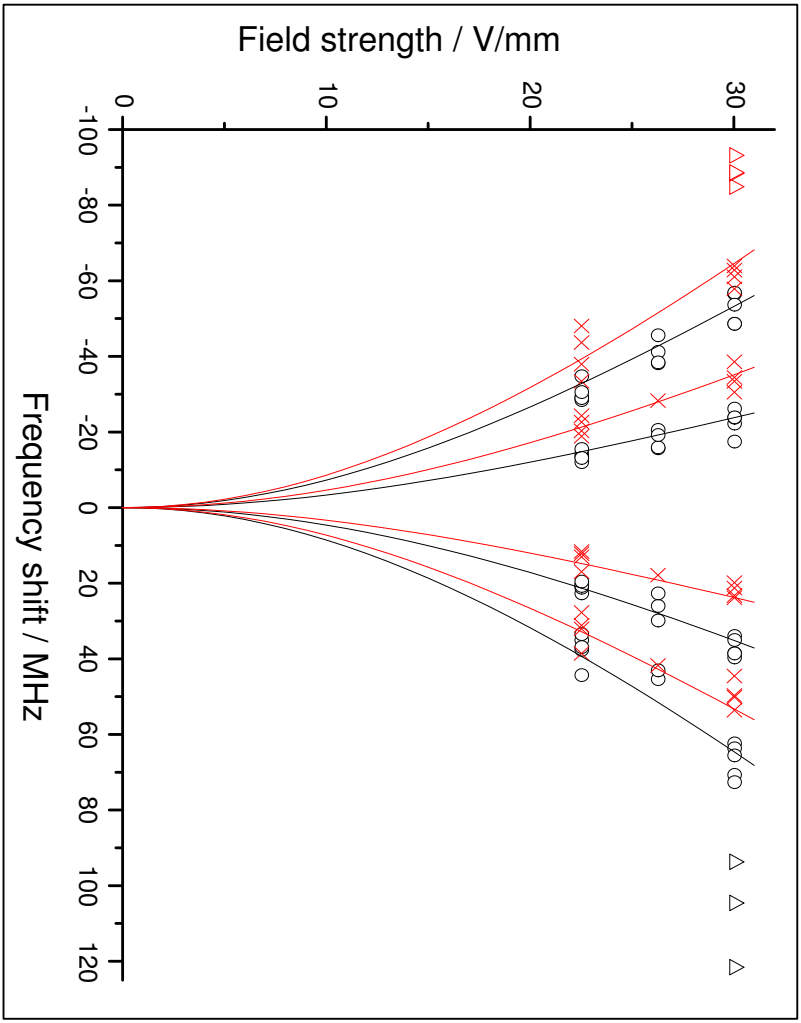

Figure 4.9: Observed transitions as shown in fig. 4.8 vs. electric field amplitude. The circles in black indicate transitions where the direction of circular polarization was the same as that of the driving-field rotation, see table 4.1, whereas the red crosses show the opposite case referring to the table 4.2. The triangles indicate non-assigned transitions.

Chapter 5

Relation of the RFS to some other effects

5.1 Berry Phase

There are some similarities between the Berry phase [27] and the rotational frequency shift. The Berry phase is a phase appearing in addition to the dynamical phase of a quantum state, when some periodic external coupling parameter is varying slowly (adiabatically). The additional phase can, however, be interpreted as an energy shift [28], when the eigenvalues of the system do not change with the varying parameter. This is the case when a rotating external field takes the role of the parameter [29, 30]. We can apply the RFS procedure, transform the system into the co-rotating frame and solve the eigenvalue problem. The eigenvalues (energies) are then shifted due to the RFS. On the other hand, we can interpret these shifts as a manifestation of the Berry phase. The relations have been schematically depicted in fig. 5.1. A more quantitative consideration for a system in a rotating environment is presented as follows. Let

$$\Psi(\mathbf{r},t) = \exp(-\frac{i}{\hbar}\xi(t))\Psi(\mathbf{r}) \tag{5.1}$$

be an eigenstate of the hamiltonian

$$H(\phi) = H_0 + \widehat{A}(\phi), \tag{5.2}$$

where $\widehat{A}(\phi)$ is an operator describing an external vector field in the xy-plane, and ϕ is the angle between the field direction and the x-axis. Let the field rotate with the angular frequency Ω, which implies $\phi = \Omega t$. Berry [27] showed that for a slow (adiabatic) field rotation the dynamical phase can be written

$$\xi(t) = \int_0^t E(\phi)dt' - \hbar\Gamma = Et - \hbar\Gamma, \tag{5.3}$$

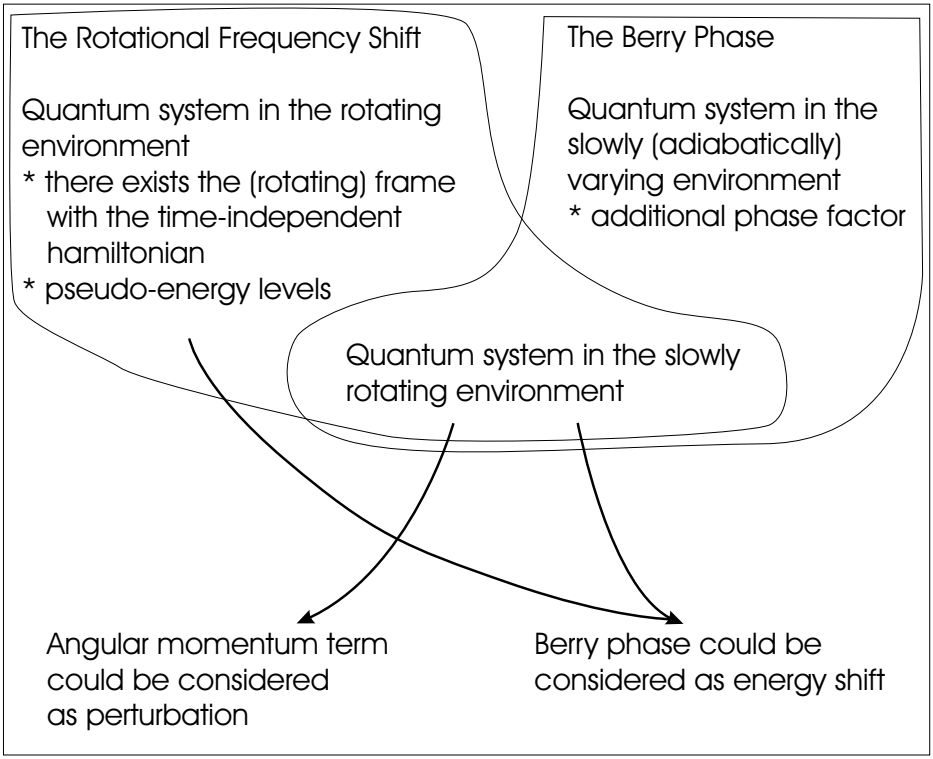

Figure 5.1: Schematic representation of the relations between the Berry phase and the rotational frequency shift.

where the first term is the dynamical phase in the static case (field not rotating), and $E(\phi)$ is an eigenstate energy of the hamiltonian $H(\phi)$. As the amplitude of the external field is assumed to be constant, $E(\phi)$ is time independent.

$$\Gamma_T = i \oint_C \langle \Psi(\mathbf{r}) | \nabla_\phi | \Psi(\mathbf{r}) \rangle \, d\phi \tag{5.4}$$

is the Berry phase accumulated in one period of the parameter change (rotation of the field), $\Gamma = \frac{t}{T}\Gamma_T$. Considering that $\xi(t)/t = E'$ is the energy of the state, we can write

$$E' = \frac{\xi(t)}{t} = E - \frac{\Gamma}{t} = E - \frac{\hbar\Gamma_T}{T} = E - \frac{\hbar\Gamma_T\Omega}{2\pi} = E + \Delta E, \tag{5.5}$$

with ΔE as the energy shift mentioned above [28]. In particular, let us consider the state

$$\Psi_m(\mathbf{r}, t) = \exp(-\frac{i}{\hbar}\xi(t))\Psi_m(\mathbf{r}), \tag{5.6}$$

where $\Psi_m(\mathbf{r})$ is an eigenstate of the angular momentum operator along some axis z', and $m = \pm\frac{1}{2}n$, $n = 0, 1, 2, \ldots$. In this case the Berry phase is

$$\Gamma_T = i \int_0^{2\pi} \langle \Psi_m(\mathbf{r}) | \frac{\partial}{\partial \phi} | \Psi_m(\mathbf{r}) \rangle \, d\phi =$$

$$- \int_0^{2\pi} \langle \Psi_m(\mathbf{r}) | \, L_z \, | \Psi_m(\mathbf{r}) \rangle \, d\phi = -2\pi m \cos(\alpha), \tag{5.7}$$

where α means the angle between the z' and z axes. Comparing equations 5.7 and 5.5 we get

$$\Delta E = \hbar \Omega m \cos(\alpha). \tag{5.8}$$

We could observe this energy shift in the form of

$$\Delta E_{obs} = \pm \hbar \Omega \cos(\alpha) \tag{5.9}$$

with the aid of spectroscopic electromagnetic dipole transitions $\Delta m = \pm 1$, A special case is considered in the next paragraph.

5.1.1 Quadrupole nuclear resonance with a rotating sample - strong field RFS

As an example we consider the spin $\frac{3}{2}$ nucleus of ^{35}Cl in a $NaClO_3$ crystal. Tycko [28] has investigated experimentally the resonance line splitting caused by crystal rotation, and interpreted as the manifestation of the Berry phase. In this paragraph, the experiment will be discussed in the framework of the RFS.

The hamiltonian of such a nuclear spin in zero magnetic field simply reads

$$H = \omega_Q S_s^2 \tag{5.10}$$

where S is the spin operator, s denotes the direction of the crystal axis, and ω_Q is a coupling constant. The eigenvalues of the hamiltonian H are

$$\begin{aligned} E_1 = E_3 &= \frac{1}{4}\hbar\omega_Q, \\ E_2 = E_4 &= \frac{9}{4}\hbar\omega_Q, \end{aligned} \tag{5.11}$$

and the transition angular frequency is

$$\omega_0 = 2\omega_Q. \tag{5.12}$$

When we rotate the crystal, we have to use

$$S_s = S_z \cos\alpha + S_x \sin\alpha \cos\Omega t + S_y \sin\alpha \sin\Omega t, \tag{5.13}$$

where α is the angle between the rotational axis z and the crystal axis. In the experiment, α was chosen as the *magic angle*, $\cos^2\alpha = \frac{1}{3}$. Considering the crystal in the co-rotating frame, the hamiltonian H' takes the form

$$H' = \omega_Q S'^2 + \Omega S_z, \tag{5.14}$$

where the spin operator S' reads [1]

$$S' = S_z\cos\alpha + S_x\sin\alpha =$$
$$\frac{\hbar\cos\alpha}{2}\begin{pmatrix} 3 & 0 & 0 & 0 \\ 0 & 1 & 0 & 0 \\ 0 & 0 & -1 & 0 \\ 0 & 0 & 0 & -3 \end{pmatrix} + \frac{\hbar\sin\alpha}{2}\begin{pmatrix} 0 & \sqrt{3} & 0 & 0 \\ \sqrt{3} & 0 & 2 & 0 \\ 0 & 2 & 0 & \sqrt{3} \\ 0 & 0 & \sqrt{3} & 0 \end{pmatrix}. \tag{5.15}$$

Setting $\cos^2\alpha = \frac{1}{3}$ it follows

$$H' = \frac{\hbar\omega_Q}{4}\begin{pmatrix} 5 & 4\sqrt{\frac{2}{3}} & \frac{4}{\sqrt{3}} & 0 \\ 4\sqrt{\frac{2}{3}} & 5 & 0 & \frac{4}{\sqrt{3}} \\ \frac{4}{\sqrt{3}} & 0 & 5 & -4\sqrt{\frac{2}{3}} \\ 0 & \frac{4}{\sqrt{3}} & -4\sqrt{\frac{2}{3}} & 5 \end{pmatrix} + \frac{\hbar\Omega}{2}\begin{pmatrix} 3 & 0 & 0 & 0 \\ 0 & 1 & 0 & 0 \\ 0 & 0 & -1 & 0 \\ 0 & 0 & 0 & -3 \end{pmatrix}. \tag{5.16}$$

The pseudo-energy levels are

$$\begin{aligned} E'_1 &= \frac{1}{4}\left(5\hbar\omega_Q - 2\sqrt{4\hbar^2\omega_Q^2 + 5\hbar^2\Omega^2 - 4\hbar\Omega\sqrt{\hbar^2\Omega^2 + 3\hbar^2\omega_Q^2}}\right), \\ E'_2 &= \frac{1}{4}\left(5\hbar\omega_Q + 2\sqrt{4\hbar^2\omega_Q^2 + 5\hbar^2\Omega^2 - 4\hbar\Omega\sqrt{\hbar^2\Omega^2 + 3\hbar^2\omega_Q^2}}\right), \\ E'_3 &= \frac{1}{4}\left(5\hbar\omega_Q - 2\sqrt{4\hbar^2\omega_Q^2 + 5\hbar^2\Omega^2 + 4\hbar\Omega\sqrt{\hbar^2\Omega^2 + 3\hbar^2\omega_Q^2}}\right), \\ E'_4 &= \frac{1}{4}\left(5\hbar\omega_Q + 2\sqrt{4\hbar^2\omega_Q^2 + 5\hbar^2\Omega^2 + 4\hbar\Omega\sqrt{\hbar^2\Omega^2 + 3\hbar^2\omega_Q^2}}\right). \end{aligned} \tag{5.17}$$

For $\Omega \ll \omega_Q$

$$E'_1 \simeq \frac{1}{4}\hbar\omega_Q + \frac{\sqrt{3}}{2}\hbar\Omega + O(\hbar^2\Omega^2),$$

[1] Pauli matrices for spins greater than $\frac{1}{2}$ are not easy to find in the literature in their explicit form. The present author collected them for spins up to 2 in [26]. They can be easily calculated using general formulae: $S_z|s,m_s\rangle = m_s|s,m_s\rangle$, $S_+|s,m_s\rangle = \sqrt{s(s+1) - m_s(m_s+1)}\,|s,m_s+1\rangle$, $S_-|s,m_s\rangle = \sqrt{s(s+1) - m_s(m_s-1)}\,|s,m_s-1\rangle$, $S_x = \frac{1}{2}(S_+ + S_-)$ and $S_y = \frac{i}{2}(S_+ - S_-)$, see for example [31]

$$
\begin{aligned}
E'_2 &\simeq \frac{9}{4}\hbar\omega_Q - \frac{\sqrt{3}}{2}\hbar\Omega + O(\hbar^2\Omega^2),\\
E'_3 &\simeq \frac{1}{4}\hbar\omega_Q - \frac{\sqrt{3}}{2}\hbar\Omega + O(\hbar^2\Omega^2),\\
E'_4 &\simeq \frac{9}{4}\hbar\omega_Q + \frac{\sqrt{3}}{2}\hbar\Omega + O(\hbar^2\Omega^2),
\end{aligned}
\tag{5.18}
$$

and the transition angular frequencies in the rotating frame are

$$
\begin{aligned}
\omega'_1 &= \frac{1}{\hbar}(E'_2 - E'_1) = 2\omega_Q - \sqrt{3}\Omega,\\
\omega'_2 &= \frac{1}{\hbar}(E'_4 - E'_3) = 2\omega_Q + \sqrt{3}\Omega,\\
\omega'_3 &= \frac{1}{\hbar}(E'_2 - E'_3) = 2\omega_Q,\\
\omega'_4 &= \frac{1}{\hbar}(E'_4 - E'_1) = 2\omega_Q = \omega'_3.
\end{aligned}
\tag{5.19}
$$

As the ac-magnetic resonant field oscillates in the direction of the rotation axis, its frequency remains unchanged when transforming between laboratory and rotating frames [2]. Hence we have

$$
\begin{aligned}
\omega_1 &= \omega_0 - \sqrt{3}\Omega,\\
\omega_2 &= \omega_0 + \sqrt{3}\Omega,\\
\omega_3 &= \omega_4 = \omega_0.
\end{aligned}
\tag{5.20}
$$

This result confirms the Berry phase interpretation of the experimental results described in [28], from the point of view of the rotational frequency shift. Since no assumption about the adiabaticity of the rotation has been made, the theoretical predictions in eqs. 5.17 are more general than those obtained from the Berry phase approach [28]. As the rotation frequency achieved in TYCKO's experiment is much smaller than the coupling between the nuclear spins and the crystal field, we have $\hbar\Omega \ll \hbar\omega_Q$, and the system shows the *strong field* case RFS.

5.2 The dressed state approach

The dressed state approach has been developed for the theoretical description of quantum systems, such as atoms, in laser fields. Citing from [32]:

> *'The motivation for such a quantum treatment is (...) the Hamiltonian of the atom + field global system is time independent, it is possible to introduce true energy levels.'*

[2] Different from the other experiments described in this work, where the electromagnetic field frequency transforms in a non-trivial way.

The motivation for this approach is similar to the one behind the RFS: one wants to remove the time-dependency of the hamiltonian. Whereas in the dressed state framework the laser field has to be considered quantized, in the RFS approach a geometrical coordinate transformation is employed. The contact point of these two approaches is the case of the atom in a circularly polarized laser field, as already discussed in sec. 3.3.

5.3 Rotation as a fictitious magnetic field

It is well known that there are analogies between a rotation and a magnetic field. However, there are also some differences. Consider a molecular quantum system subject to a magnetic field along the z-axis. The effective hamiltonian is then

$$H_{mag} = H_0 - g_L L_z B - g_S S_z B - g_N N_z B - g_P P_z B - ..., \qquad (5.21)$$

where L, S, N and P are the angular momentum operators for the orbiting electron, the electronic spin, nuclear spin, and the rotating nuclear frame, respectively. g_L, g_S, g_N and g_P are the associated g-factors and could be considered constant in a given quantum state. Let us compare it with the hamiltonian obtained after transformation into a rotating frame:

$$H_{rot} = H_0 - \Omega L_z - \Omega S_z - \Omega N_z - \Omega P_z - ... = H_0 - \Omega(L_z + S_z + N_z + P_z + ...). \qquad (5.22)$$

It is obvious that all angular momentum operators are multiplied by one parameter, the rotational frequency. Oppositely, eq. 5.21 cannot be re-written in the form of eq. 5.22, because the g-factors are in general different for each rotational degree of freedom.

One can illustrate this with a simple example. Consider a classical electron moving in an orbit around its nucleus, and spinning around an intrinsic axis (classical spin). It is possible to find a frame in which the electron is at rest, and there exists another frame, in which the electron does not spin. But in general these are different - there is no frame with a non-spinning electron at rest.

It would be interesting to perform the experiment stressing the difference between the magnetic field and the rotation. The idea would be similar to the experiments performed in this work, but involving a rotating *magnetic* field instead of an electric one, coupling with the quantum system containing different kinds of magnetic moment.

5.4 Sagnac Effect

The standard version of the Sagnac interferometer [33, 34], shown in fig. 5.2a, is used in practice in the form of the *laser gyroscope* [33]. When rotated, the detector registers a change of the output intensity due to the changed interferometer

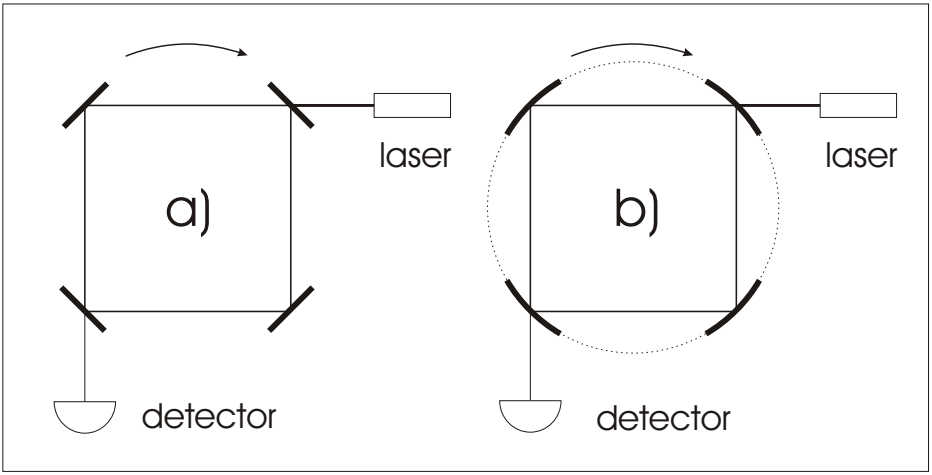

Figure 5.2: Two variants of the Sagnac interferometer: a) original version; b) spherically symmetric version.

condition. If one replaced the laser light mode inside the Sagnac interferometer by an atomic electron wave function [35], the interferometer mirrors would play the role of a potential. However, in the traditional Sagnac interferometer (fig. 5.2a) the mirrors are flat, so that the interferometer is *not* spherically symmetric like the atomic analogue. Since the atomic Coulomb potential is spherically symmetric, it turns out that the traditional Sagnac interferometer is rather the analog of an atom in an external lateral field, which breaks the rotational symmetry. As we know that rotational symmetry breaking is crucial for observing any effect in the laboratory frame [2], we can conclude immediately that a spherically symmetric Sagnac interferometer such as shown in fig. 5.2b would not be sensitive to rotation[3]. As the external field in RFS is a continuous variable, we can imagine different versions of spherically nonsymmetric Sagnac interferometers, with different sensitivities to rotation. An *almost* symmetric one would be similar to the complete symmetric form in fig. 5.2b, but with slightly differing shapes of the interferometer mirrors.

[3] when not filled with some medium, i.e. glass

Summary

The rotational frequency shift (RFS) has been investigated. The existence of the RFS, previously proposed [2], has been explicitly demonstrated experimentally for the first time, for different quantum systems and frequency regimes. Suitable laser spectroscopical experiments have been designed, and performed with atomic and molecular quantum systems. The *fast rotation*-RFS has been verified for atomic lithium. In this experiment, the electric field of a circularly polarized strong laser beam has been employed as the rotating environment. The spectra have been analyzed first using the concept of the *dynamic Stark effect*, and then using that of the rotational frequency shift. The most interesting *intermediate*-RFS case has been demonstrated with the aid of the thioformaldehyde molecule which was exposed to a rotating radio frequency electric field. The existence of the *strong field*-RFS has been shown by reanalyzing an already existing experiment [28]. Finally, the relation between the *strong field*-RFS and the Berry phase has been discussed, and the dressed state method, the fictitious magnetic field, and the Sagnac effect have been considered in the light of the rotational frequency shift procedure.

Zusammenfassung

In dieser Arbeit wurde die Rotationsfrequenzverschiebung (rotational frequency shift, RFS) untersucht. Die Existenz dieses Phänomens, vorgeschlagen in [2], konnte zum ersten Mal experimentell demonstriert werden - explizit für verschiedene Quantensysteme und Frequenzgebiete. Die benötigten hochauflösenden laserspektroskopischen Experimente wurden für atomare und molekulare Quantensysteme entworfen und durchgeführt. Der Fall der schnellen Rotation (*fast rotation*-RFS) wurde am atomaren Lithium demonstriert. Hier wurde das elektrische Feld einer zirkular polariesierten, starken Laserstrahls als rotierende Umgebung eingesetzt. Die Spektren wurden vergleichend mit Hilfe des dynamischen Stark-Effekts und der RFS-Methode analysiert. Die moderat schnelle Rotation (*intermediate*-RFS) ist der interessanteste Fall. Er wurde am Thioformaldehyd-Molekül verifiziert, in einem rotierenden Radiofrequenzfeld. Der *strong field*-RFS Fall wurde anhand einer Reanalyse eines bereits existierenden Experiments [28] erläutert. Es wurde dann aufgezeigt, dass eine bemerkenswerte Verwandtschaft zwischen dem *strong field*-RFS und der Berry-Phase besteht. Zum Schluss wurden in ähnlicher Weise die sogenannten *dressed states*, das fiktive Magnetfeld und der Sagnaceffekt mit der Rotationsfrequenzverschiebung in Zusammenhang gebracht.

Appendix A

Experimental details

A.1 Evaluation of the effect-modulation signals

It is non-trivial to analyze the effect-modulation spectra in a useful way when the frequency shifts are smaller then the linewidth. In the effect-modulated experiment we typically record the difference between two such profiles, which leads to the shapes shown in fig. A.1. The distance between the minimum and the maximum of such a curve decreases with decreasing shift, but for the small shifts it saturates, which is shown in figure A.2. So, it is not useful to rely on the distance of the two extremes for small shifts below the fwhm. It is much better to utilize the amplitude (maximum hight of the curve) for analyzing the small shifts. Figure A.3 shows the dependence of the difference signal amplitude on the frequency shift. For small shifts the normalized height of the curve is

$$A(\Delta\nu) \simeq \frac{3\sqrt{3}}{4}\Delta\nu - O(\Delta\nu^3), \tag{A.1}$$

for $\Delta\nu$ in units of fwhm. The reversed formula

$$\Delta\nu \simeq \frac{4\sqrt{3}}{9}A(\Delta\nu) \tag{A.2}$$

has been used for the evaluation of the frequency shifts in the experiments described in sec. 4.2.2, where the frequency shifts amounted to typically a percent of the fwhm. The evaluation error was determined by the amplitude readout error δA:

$$\delta\Delta\nu = \frac{4\sqrt{3}}{9}\delta A. \tag{A.3}$$

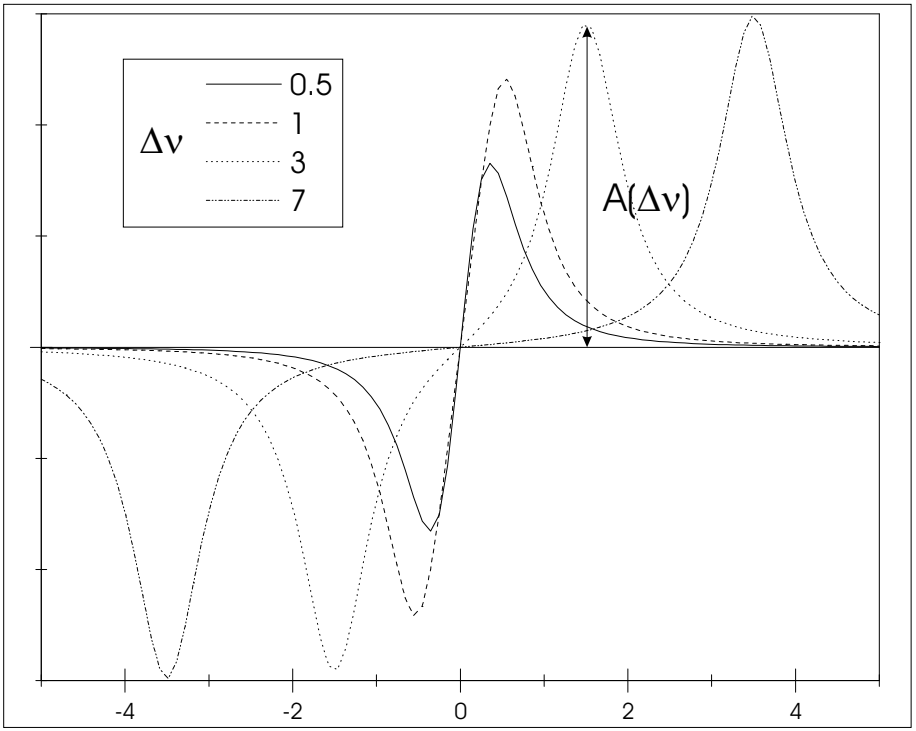

Figure A.1: The amplitude differences between two Lorentz profiles for different shifts 0.5, 1, 3 and 7 in units of fwhm.

A.2 Production of circularly polarized light

Circular polarized light can be obtained when linearly polarized light is guided through a $\lambda/4$-retarder, and its optical axis is oriented 45° with respect to the axis of linear polarization. The retarder can be made of birefringent material (for example mica), or uses total internal reflection (Fresnel rhomb). Fresnel $\lambda/4$ rhombs are inconvenient, because they cause a displacement of the light beam. The problem with birefringent retarders is that their retardation depends on the wavelength. One needs, therefore, for each wavelength a matched retarder plate. Another possibility is to utilize a Babinet-Soleil-compensator [33]. It consists of two wedges of birefringent material, one of them movable. The retardation factor can then be adjusted by changing the thickness of the material. To do this one needs the setup shown in figure A.4. One guides the laser beam through the polarization filter, the compensator, and the cell assembly. The beam is reflected

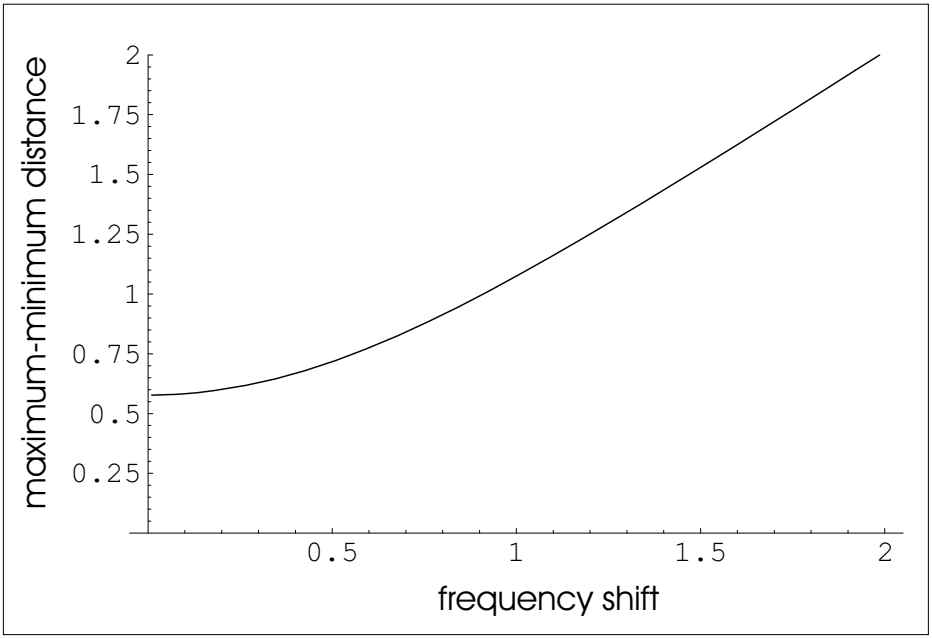

Figure A.2: The distance between the maximum and minimum of the difference signal vs. the frequency shift, compare fig. A.1. Both axes are in units of the fwhm of the Lorentz profile.

back on a slightly different path to see the back-reflected beam spot on the iris diaphragm. If the retarder (Babinet-Soleil-compensator) is adjusted exactly to $\lambda/4$, the back beam is retarded by $\lambda/2$, meaning that the polarization is linear and rotated by 90 degrees, so it cannot pass the polarization filter, and the back beam spot on the iris diaphragm disappears.

A.3 Production of the rotating electric field

> The constructive part described in this section has been worked out and realized by H. Schimming and G. Klose.

Providing the rotating electric field suitable for observation of the RFS in a molecular system was the greatest technical challenge of this work. The minimum frequency shift had to be an order of magnitude greater than the spectroscopic linewidth, requiring at least about 50 MHz. The minimum distance between the electrodes and correspondingly maximum field strength was restricted by requirements of the field homogeneity and electrical capacity between the electrodes,

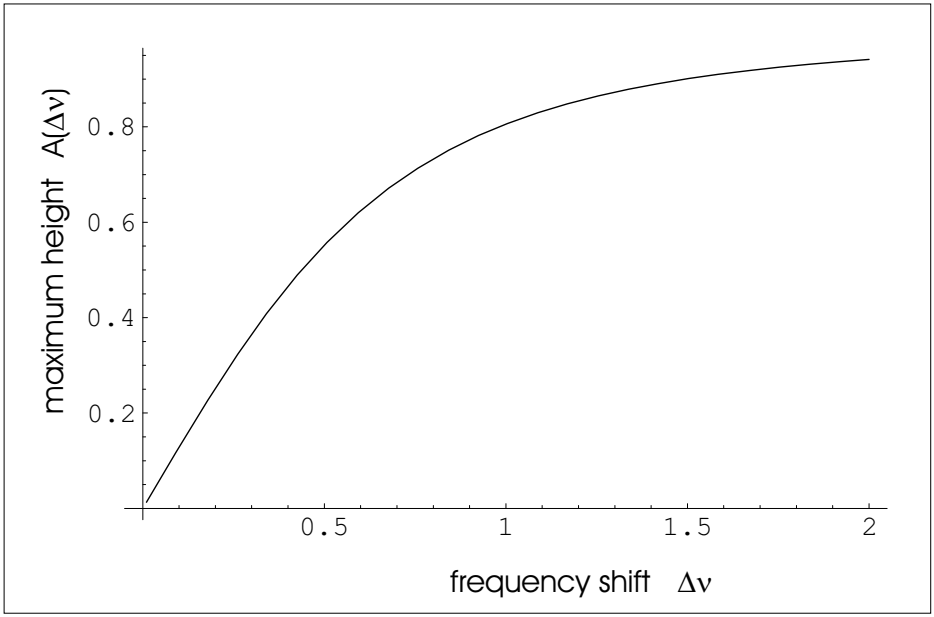

Figure A.3: Maximum height of the difference signal vs. frequency shift. The frequency is given in units of fwhm of the Lorentz profile, and the height relative to the height of the unperturbed Lorentz curve.

fixing it to a few millimeters. The *intermediate*-RFS needed a field amplitude of at least 15 V/mm for 50 MHz, increasing linearly with the frequency. This ended up in a voltage amplitude between the electrodes of the order of 100 V. Initial considerations showed that simply driving the electrode system by an alternating voltage would require a power of about 100 W. Though amplifiers for such demands are available from radio communication emitters, the power would dissipate in the form of heat, and cooling of a compact quadrupole in the vacuum chamber would not be easy. It was, therefore, decided to incorporate the electrode pairs as part of an LC resonator. This reduced the required electrical power significantly, but fixed the field frequency to the arbitrarily chosen value of 80.63 MHz.

Figure A.5 shows the general diagram of the electronic circuit. Photographs of the circuit are provided in figs. A.8 - A.10. The sinusoidal signal from the generator is split and passes through the emitter followers in order to separate the driving circuits for the two plate pairs. A transformative coupled band filter was included in one of them in order to achieve the 90 degrees phase difference between the plate pairs. The amplified signals are coupled, via transformers, to the LC resonators containing the electrodes. The four final stage amplifiers are

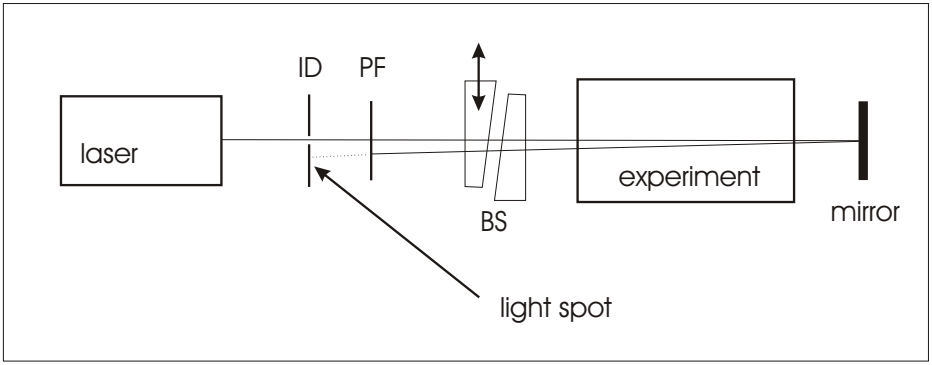

Figure A.4: Arrangement for the production of circularly polarized light. ID - iris diaphragm, PF - polarization filter, BS - Babinet-Soleil compensator.

used to increase the amplitude. A detailed diagram of these couplers is shown in fig. A.6. The amplitude is monitored by capacitive splitters of ratio 500 : 1, one for each electrode, and connected to the oscilloscope, see fig. A.7. The oscilloscope displays the voltage difference between each pair. The transistors built in emitter followers are of the type 2N3866, these in the amplifiers are 2SC2910. All coils, which can be clearly seen on photographs, are of the inductance of 160 nH.

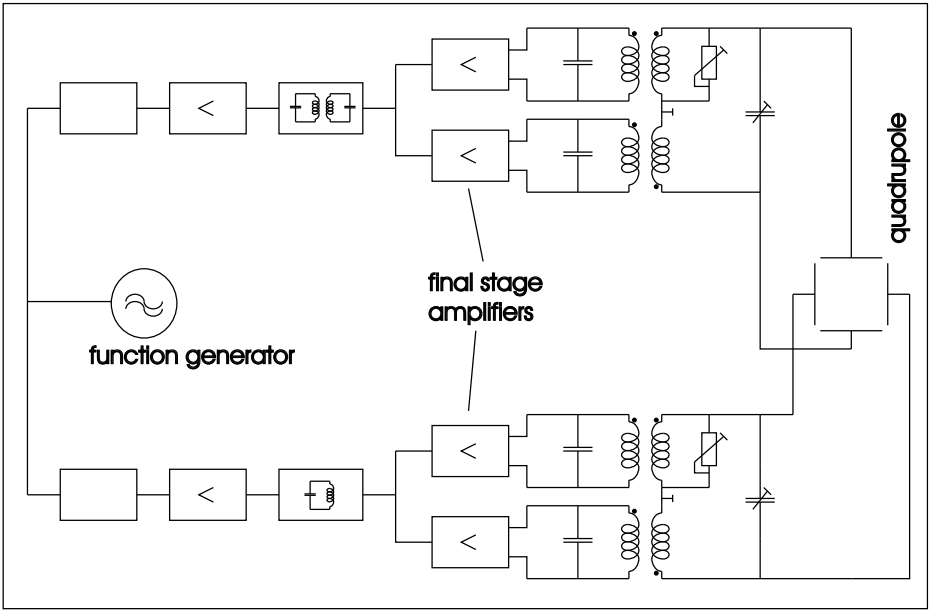

Figure A.5: Block diagram of the electronic circuit providing the rotating electric field. Details are shown on the following figures.

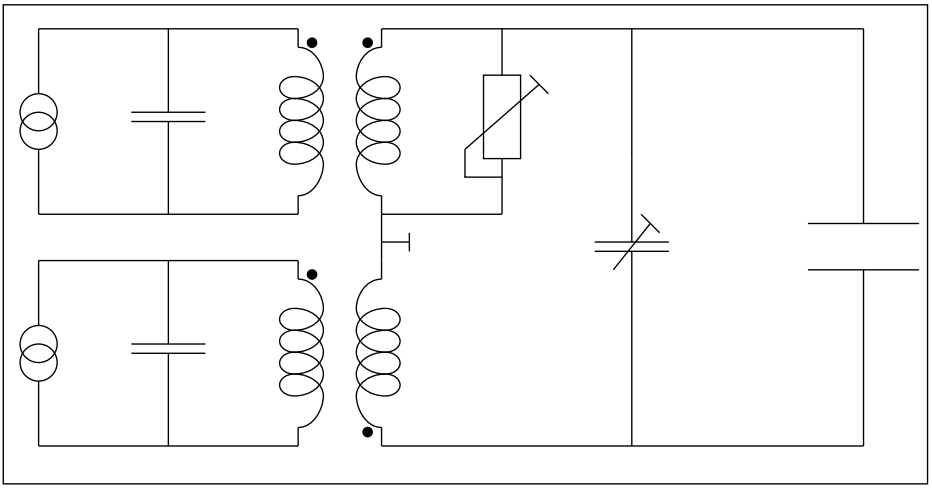

Figure A.6: The tansformative coupler.

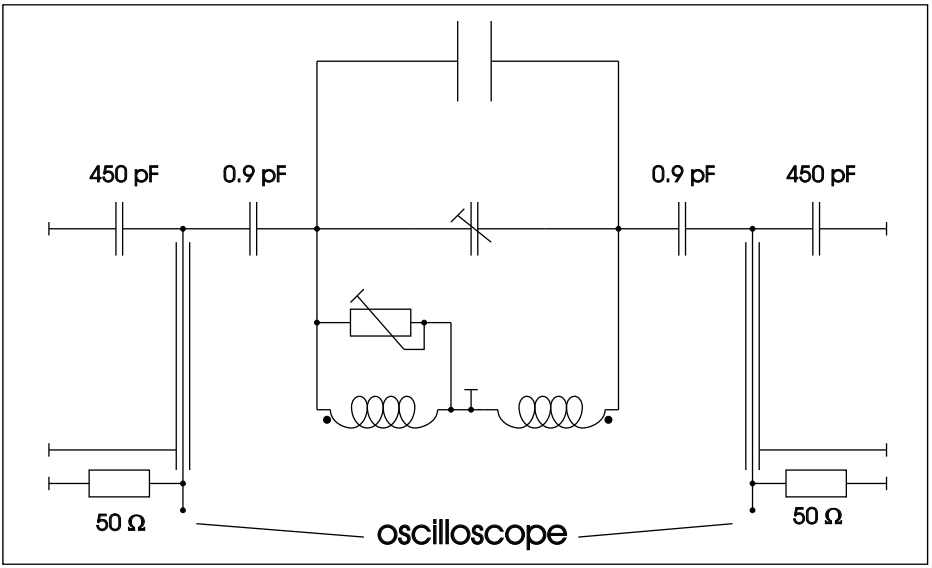

Figure A.7: Capacitive splitter for measuring the field amplitude.

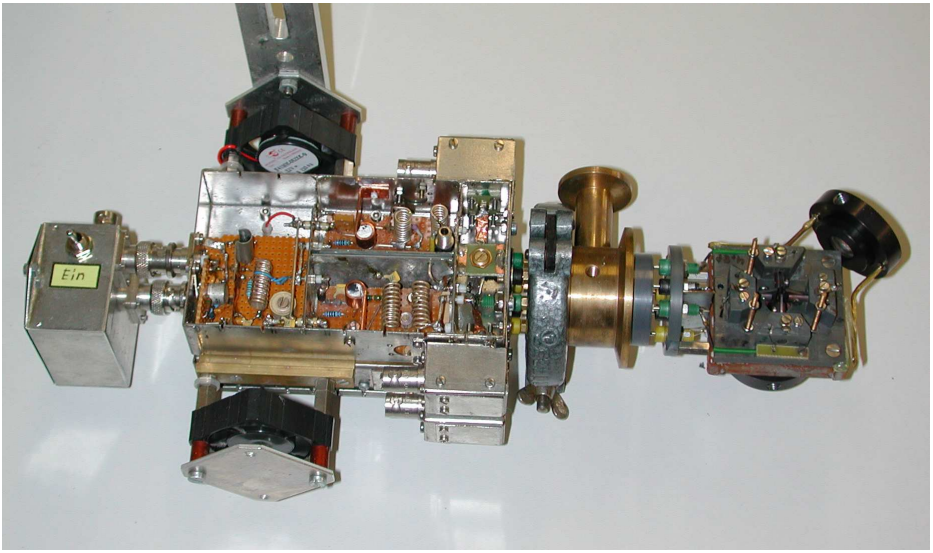

Figure A.8: General view of the driver circuit with the vacuum port and quadrupole on the right side.

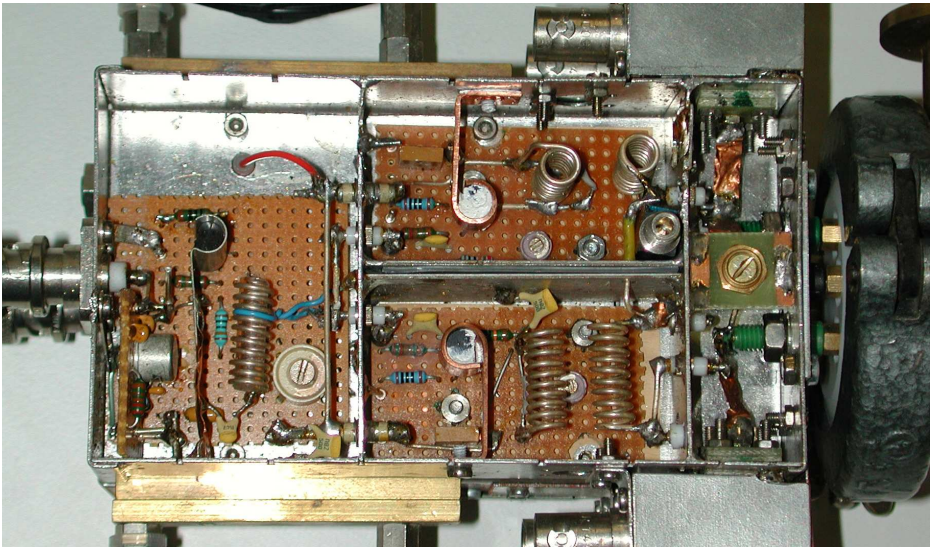

Figure A.9: Detailed view of the driver circuit for one electrode pair. This picture refers to the bottom part of fig. A.5.

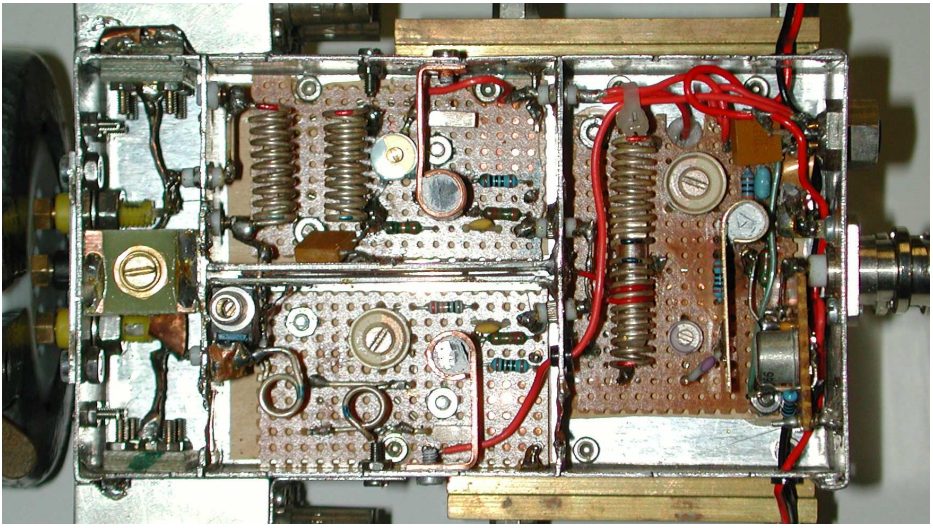

Figure A.10: Detailed view of the driver circuit for one electrode pair. This picture refers to the upper part of fig. A.5.

Bibliography

[1] Ch. Doppler, *Über das farbige Licht der Doppelsterne und einiger anderer Gestirne des Himmels*, Abh. der Königl. Böhm. Ges. der Wiss., Bd. II Nr. 5, 1842

[2] I. Białynicki-Birula, Z. Białynicka-Birula, *Rotational Frequency Shift*, Phys. Rev. Lett., **78**, 2539 (1997)

[3] J. Courtial, K. Dholakia, D. A. Robertson, L. Allen, M. J. Padgett, *Measurement of Rotational Frequency Shift Imparted to a Rotating Light Beam Possessing Orbital Angular Momentum*, Phys. Rev. Lett., **80**, 3217 (1998)

[4] J. Courtial, K. Dholakia, D. A. Robertson, L. Allen, M. J. Padgett, *Rotational Frequency Shift of a Light Beam*, Phys. Rev. Lett., **81**, 4828 (1998)

[5] L. Allen, M. J. Padgett, M. Babiker, *The Orbital Angular Momentum of Light*, Progress in Optics, **XXXIX**, 291 (1999)

[6] J. D. Anderson et. al., *Study of anomalous acceleration of Pioneer 10 and 11*, Phys. Rev. D, **65**, 082004 (2002)

[7] J. D. Anderson, B. Mashhoon, *Pioneer Anomaly and the Helicity-Rotation Coupling*, `arXiv:gr-qc/0306024`

[8] J. P. Mbelek, M. Michalski, *Can conventional forces really explain the anomalous acceleration of Pioneer 10/11?*, Int. J. Mod. Phys. D, **13**, 865 (2004)

[9] N. Ashby, *Relativity in the Global Positioning System*, Living Reviews in Relativity, **6**, 1 (2003)

[10] P. F. Liao, J. E. Bjorkholm, *Direct Observation of Atomic Energy Level Shifts in Two-Photon Absorption*, Phys. Rev. Lett., **34**, 1 (1975)

[11] C. Cohen-Tannoudji, J. Dupont-Roc, *Experimental Study of Zeeman Light Shifts in Weak Magnetic Fields*, Phys. Rev. A, **5**, 968 (1972)

[12] D. Cho, J. of Kor. Phys. Soc., **30**, 373 (1997)

[13] C. Y. Park, H. Noh, C. M. Lee, D. Cho, *Measurement of the Zeeman-like ac Stark shift*, Phys. Rev. A, **63**, 032512 (2001)

[14] M. Rosatzin, D. Suter, J. Mlynek, *Light-shift-induced spin echoes in $J = \frac{1}{2}$ atomic ground state*, Phys. Rev. A, **42**, R1839 (1990)

[15] M. Zielonkowski, J. Steiger et. al., *Optically induced spin precession and echo in an atomic beam*, Phys. Rev. A, **58**, 3993 (1998)

[16] C. Y. Park, J. Y. Kim, J. M. Song, D. Cho, *Optical Stern-Gerlach effect from the Zeeman-like ac Stark shift* , Phys. Rev. A, **65**, 033410 (2002)

[17] H. A. Bethe, E. E. Salpeter, *Quantum mechanics of one- and two-electron atoms*, A Plenum/Rosetta Edition, 1977, ISBN 0-306-20022-8

[18] A. Peres, D. R. Terno, *Quantum information and relativity theory*, Rev. Mod. Phys., **76**, 93 (2004)

[19] W. Demtröder, *Laser Spectroscopy. Basic Concepts and Instrumentation*, Springer Verlag, 2000, ISBN 3-5405-7171-X) (or german version *Laserpektroskopie. Grundlagen und Techniken* , Springer Verlag, 2000, ISBN 3-5406-4219-6

[20] K. H. Fung, D. A. Ramsay, *Doppler-free Stark Spectra of the 4_0^1 band of the $\tilde{A}\ ^1A_2$ system of thioformaldehyde*, Mol. Phys., **88**, 997 (1996)

[21] Walter Gordy, Robert L. Cook, *Microwave Molecular Spectra*, John Wiley & Sons, 1984, ISBN 0-471-08681-9

[22] B. Fabricant, D. Krieger, J. S. Muenter, *Molecular beam electric resonance study of formaldehyde, thioformaldehyde and ketene*, J. Chem. Phys., **67**, 1576 (1977)

[23] P. Otto, *Atomare diamagnetische Suszeptibilitäten angeregter Elektronenzustände mittels dopplerfreien Zweiphotonenspektroskopie* , Ph. D. thesis, Shaker Verlag, 1999, ISBN 3-8265-6704-8

[24] P. Otto, M. Gamperling, M. Hofacker, T. Meyer, V. Pagliari, A. Stifter, M. Krauss, W. Hüttner, *Level magnetizabilities of the alkaline metal atoms*, Chem. Phys., **282**, 289 (2002)

[25] W. I. McAlexander, E. R. I. Abraham and R. G. Hulet, *Radiative lifetime of the 2P state of lithium*, Phys. Rev. A, **54**, R5 (1996)

[26] M. Michalski, *Rotacyjne przesunięcie częstości*, 1999, M. Sc. thesis (in Polish)

[27] M. V. Berry, *Quantal phase factors accompanying adiabatic changes*, Proc. R. Soc. A, **392**, 45 (1984)

[28] R. Tycko, *Adiabatic Rotational Splittings and Berry's Phase in Nuclear Quadrupole Resonance*, Phys. Rev. Lett., **58**, 2281 (1987)

[29] Shi-Min Cui, Hong-Hua Xu, *Berry's phase in rotating systems*, Phys. Rev. A, **44**, 3343 (1991)

[30] Shi-Min Cui, *Nonadiabatic Berry phase in rotating systems*, Phys. Rev. A, **45**, 5255 (1992)

[31] P. W. Atkins, R. D. Friedman, *Molecular Quantum Mechanics, Third Edition*, Oxford University Press, 1997, ISBN 0-19-855947-X

[32] C. Cohen-Tannoudji, J. Dupont-Roc, G. Grynberg, *Atom-Photon Interactions*, John Wiley & Sons, Inc., 1992, ISBN 0-471-62556-6, Chapter VI

[33] E. Hecht, *Optics*, Addison-Wesley Publishing Company, Inc., 1990, ISBN 0-201-11609-X

[34] E. J. Post, *Sagnac Effect*, Rev. Mod. Phys., **39**, 475 (1967)

[35] remark of W. Schleich

Acknowledgements

I would like to thank

- Professor Wolfgang Hüttner for letting me perform research in his institute, for revising my thesis and his support,
- Professors Iwo Białynicki-Birula and Zofia Białynicka-Birula, inventors of the Rotational Frequency Shift, for stimulating discussions,
- H. Schimming and G. Klose from the university scientific workshop for constructing the quadrupole driver electronics,
- Dr. M. Wagner for the practical introduction into laser spectroscopy, experimental work advices and assistance,
- Professors W. Kreiner and H. Jones for the loan of numerous devices,
- K-H. Peting and M. Elsner for currently supervising and repairing the electronic equipment, M. Ferner for developing and implementing a valuable LabView data acquisition program,
- Mrs. I. Gessler and Mrs. B. Rein for tea cooking and helping solve numerous bureaucratic tasks,
- other department members not mentioned above: H. Abdel-Karim, Prof. H-K. Bodenseh, Dr. K. Möllmann and Dr. R. Tammer,
- and all department members once again for the nice atmosphere.

Curriculum vitae

Personal data

Marcin Michalski
Johannes-Mynsinger-Weg 15
89075 Ulm
Germany

Tel.: (0731)5502164
e mail: marcin.michalski@physik.uni-ulm.de

born at 9.21.1975 in Sosnowiec/Poland
single

Education

10/1994–06/1997	Bachelor of mathematical modelling, College of Science, Warszawa
10/1997–01/2000	Master of physics, College of Science, Warszawa

Foreign stages

11/1997–08/1998	Technical University of Berlin
05/1999	National Technical University of Athens
since 02/2000	University of Ulm

Languages

polish, german, english

Employment

02/2000–03/2003	Ph. D. student (BAT IIa 1/2) at the University of Ulm, Chemical Physics Department
since 06/2003	University of Ulm, Surface Chemistry and Catalysis Department